Reevaluation of Poly(ethylene-*alt*-propylene)-*block*Polydimethylsiloxane Phase Behavior Uncovers Topological Close-Packing and Epitaxial Quasicrystal Growth

Aaron P. Lindsay, ¹ Ashish Jayaraman, ¹ Austin J. Peterson, ¹ Andreas J. Mueller, ¹ Steven Weigand, ³ Kristoffer Almdal, ⁴ Mahesh Mahanthappa, ¹ Timothy P. Lodge, ^{1,2} Frank S. Bates ¹*

¹Department of Chemical Engineering and Materials Science and ²Department of Chemistry,

University of Minnesota, Minneapolis, MN 55455, USA

³DND-CAT Synchrotron Research Center, Northwestern University, APS/ANL Building 432-A004, 9700 South Cass Ave, Argonne, Illinois 60439, USA

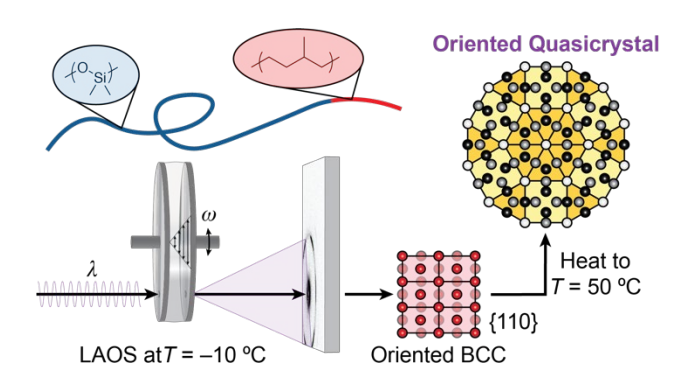
⁴Department of Chemistry, Technical University of Denmark, Kemitorvet 207, 2800 Kgs., Lyngby, Denmark

ABSTRACT

Reanalysis of an asymmetric poly(ethylene-*alt*-propylene)-*block*-polydimethylsiloxane (PEP-PDMS) diblock copolymer first investigated in 1999 has revealed a rich phase behavior including a dodecagonal quasicrystal (DDQC), a Frank-Kasper σ phase, and a body-centered cubic (BCC) packing at high temperature adjacent to the disordered state. On subjecting the sample to large amplitude oscillatory shear well below the σ -BCC order-order transition temperature (T_{OOT}), small-angle X-ray scattering evidenced the emergence of a twinned BCC phase that, on heating, underwent a phase transition to an unusually anisotropic DDQC state. Surprisingly, we observe no evidence of this apparent epitaxy on heating or cooling through the equilibrium σ -BCC transition. We rationalize these results in terms of a shear-induced order-order transition and an apparent BCC-DDQC epitaxy favored by micelle translation-mediated ordering dynamics far below T_{OOT} .

KEYWORDS: quasicrystal, block copolymer, epitaxy, shear orientation, topological close-packing, self-assembly

TOC GRAPHIC



In the past decade, several complex particle packings, including multiple Frank-Kasper (FK) phases¹-⁴ and a dodecagonal quasicrystal (DDQC),⁵ have been reported in systems comprised of self-assembled block copolymer micelles. The occurrence of such phases, characterized by topological close-packing and unit cells containing ≥ 7 particles with differing volumes and geometries, represents a striking departure from classical diblock copolymer phase behavior, wherein the high symmetry body-centered cubic (BCC) phase has long dominated the literature.⁶ Nonetheless, continued exploration of asymmetric block polymer melts and related self-assembling amphiphiles has revealed multiple routes to these complex packings, for example, *via* a reduction in molecular weight,³,7 an increase in architectural/conformational asymmetry,²,8-15 and/or blending.¹,6-25 Notably, many of these strategies are not new. Researchers have been exploring similar copolymer blends and low molecular weight amphiphiles for decades.²,6-39 However, past identification of these phases was often complicated by slow ordering kinetics and the high X-ray or neutron scattering resolution necessary to resolve their Bragg reflections.

Takagi and coworkers first identified the FK σ phase in a binary diblock copolymer/homopolymer blend^{16,17} in 2017 despite decades of intense study on blends of block copolymers with homopolymer^{26,27,32,33} and/or solvent.^{34,35} In 2019, reevaluation of hydrated poly(ethylene oxide)-*block*-polyethylene (PEO-PE) diblock co-oligomers studied extensively between 1996 and 2005^{36–38} revealed a transient, yet long-lived, FK σ phase.⁴⁰ As recently as 2020, a return to the bidisperse diblock copolymer blends widely explored in the 1990s by the Hashimoto group^{28,29,39} and others^{30,31} revealed previously unobserved DDQC, σ, and A15 packings, but only after substantial annealing periods prior to synchrotron small-angle X-ray scattering (SAXS) analysis.¹⁹ We speculated that a reevaluation of past literature under the lens of recently discovered micellar packings might reveal similar examples, hitherto hidden. Accordingly, we revisit a 1999

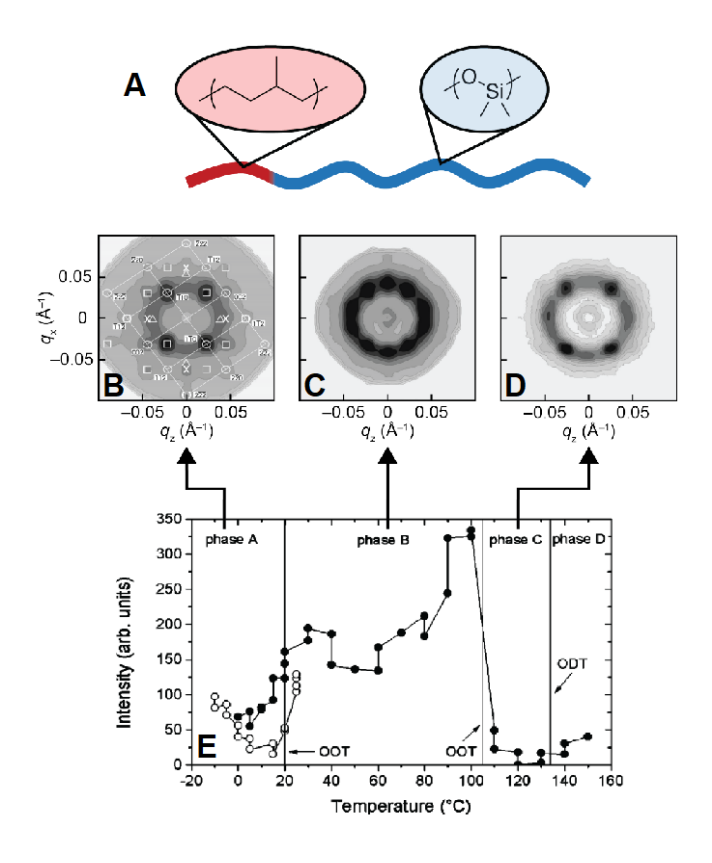


Figure 1. (A) Chemical structure of poly(ethylene-alt-propylene)-block-polydimethylsiloxane, (B-D) small-angle neutron scattering (SANS) patterns, and (E) optical transmittance data. 2D SANS patterns were collected following large amplitude oscillatory shear (LAOS) at (B) –25 °C and (D) 120 °C. Pattern (C) was collected on heating the sample from (B) to 50 °C. Optical transmittance data was obtained on cooling (closed circles) and heating (open circles) with the first and second points at shown at specific temperatures reflecting 1 and 10 h of annealing. Figures were reproduced from ref. 41, with the permission of AIP Publishing. report of an unusual progression of phases observed on cooling a low molecular weight, compositionally asymmetric poly(ethylene-alt-propylene)-block-polydimethylsiloxane (PEP-

PDMS) diblock copolymer with volume fraction $f_{PEP} = 0.22$ and molecular weight $M_n = 12.5$ kg/mol.⁴¹

As shown in Figure 1, optical birefringence and small-angle neutron scattering (SANS) measurements as a function of temperature reported by Papadakis and coworkers in 1999 revealed what appeared to be three ordered states. The intermediate ordered phase ("phase B"), which was found to be optically birefringent, displayed a single broad scattering reflection *via* SANS and lab-

source SAXS, while the high and low temperature phases appeared to order with twinned BCC symmetry. Interestingly, efforts to orient "phase B" using large amplitude oscillatory shear (LAOS) yielded an isotropic SANS pattern and a precipitous drop in the modulus. However, on heating the shear-oriented specimen (Figure 1B) to the intermediate temperature window, a 10-spot scattering pattern emerged (Figure 1C) that was incompatible with ordered-state symmetries recognized at the time. Upon reviewing these results, we concluded that the unidentified "phase B" might be the FK σ phase for 3 reasons: (1) the σ phase has a tetragonal unit cell and should therefore be optically birefringent; (2) σ is often observed at similar compositions near the particle-cylinder order-order transition (OOT);^{1,8,9} and (3) the PEP-PDMS diblock copolymer has a relatively large conformational asymmetry⁴² ($\varepsilon = (b_{\text{PEP}}/b_{\text{PDMS}})^2(\nu_{\text{PDMS}}/\nu_{\text{PEP}}) = 1.6$ where b_i and v_i represent the statistical segment length and repeat unit volume of block i determined at 140 °C) and relatively low molecular weight (M_n =12.5 kg/mol), both of which have been shown to favor σ phase formation.^{7,9}

We show herein that a reanalysis of the asymmetric PEP-PDMS diblock copolymer melt investigated by Papadakis *et al.* reaffirms the high temperature BCC phase assignment and reveals that "phase B" is, in fact, the FK σ phase. However, we found the low temperature phase behavior to differ significantly with and without applied shear. SAXS analysis following long time annealing at $T \le 25$ °C ($t_{anneal} \approx 1$ year) in conjunction with shorter periods of annealing at higher temperatures revealed σ to be the equilibrium packing for T < 110 °C; extended annealing was required below 80 °C due to kinetic limitations due to the persistence of either a DDQC state or non-ergodic liquid-like packing (LLP). Surprisingly, LAOS at -10 °C resulted in a twinned BCC phase that transitions to an anisotropically oriented DDQC morphology on heating to 50 °C. This anisotropy was lost on subsequently heating the specimen through the equilibrium σ -BCC OOT

and efforts to reproduce the observed orientational growth by cooling a shear-oriented BCC phase from 120 °C resulted in a similar loss of anisotropy on passing through the equilibrium OOT. Further, upon directly shearing a well-ordered σ phase at 80 °C, we observed a shear-induced disruption of the packing and a subsequent transition to a predominantly LLP \rightarrow DDQC $\rightarrow \sigma$ ordering pathway. We rationalize these findings in the context of a packing-dependent shear deformation behavior and an apparent BCC-DDQC epitaxy influenced by temperature-dependent ordering dynamics.

RESULTS AND DISCUSSION

In this section, we discuss the quiescent phase behavior as determined by synchrotron SAXS and dynamic mechanical analysis (DMA), after which we detail the nuances associated with the linear viscoelastic response in both the BCC and σ windows. Subsequently, we focus on the phase behavior at low temperature–first on cooling a well-ordered σ phase and then under LAOS–making reference to differences in the shear deformation behavior of σ and BCC packings found in hard materials. We then describe the growth of an anisotropic DDQC morphology upon heating a twinned BCC structure obtained by shearing the material at low temperature, evidencing an apparent BCC-DDQC epitaxy. This section concludes with a presentation and analysis of several other experiments conducted under LAOS, including the shear-induced disruption of σ and DDQC packings.

Phase Behavior. As shown in Figure 2, four distinct morphologies were obtained on quenching the sample from disorder ($T = 150 \,^{\circ}$ C). At 120 $^{\circ}$ C, we obtained a 1D scattering trace characteristic of BCC packing, which emerged rapidly (< 1 min); the presence of only two reflections can be rationalized by a form-factor extinction of the (211) peak (Figure S5) and thermal fluctuations in proximity to the ODT. At 80 $^{\circ}$ C, scattering reflections consistent with the $P4_2/mnm$ space group

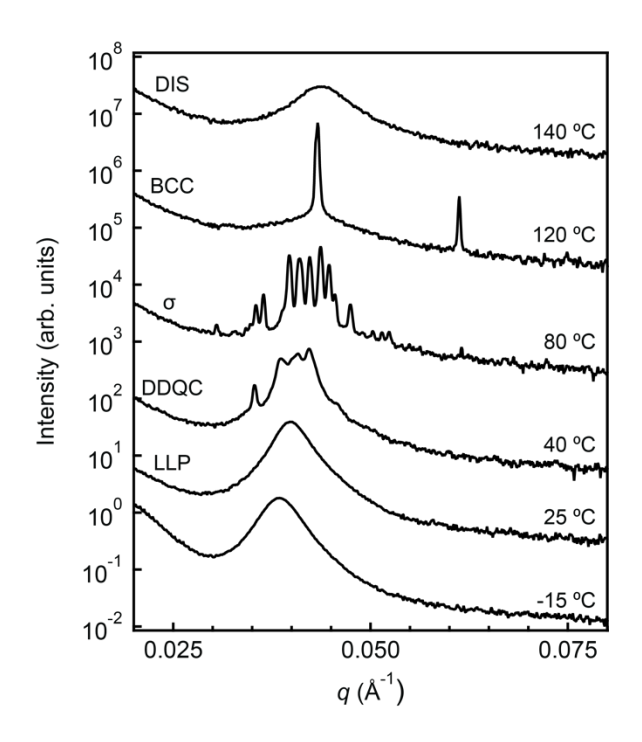


Figure 2. Vertically shifted 1D scattering profiles as a function of annealing temperature. Data were collected after rapidly cooling the sample from disorder (T = 150 °C) and annealing at T < 100 °C for 60 h. For T > 100 °C, samples were annealed for 20 min.

symmetry of a FK σ phase could be seen within 15 min (Figure S18E), giving way to more than 20 peaks after 60 h of annealing (Figure 2, Figure S6, and Table S2). Quenching to 40 °C resulted in the development of a distinctive set of three scattering peaks flanked by a sharper reflection at lower q over roughly 60 h. This pattern is associated with the DDQC state (Figure S7 and Table S3) generally observed as a metastable precursor to the σ phase. Finally, rapidly cooling the material from 150 °C to $T \le 25$ °C resulted in a disordered liquid-like packing (LLP) of micelles ($T \le 25$ °C), which was found to persist for more than 60 h of annealing at each temperature. LLP is evidenced by a broad scattering peak, similar to but narrower and more intense than that associated with the disordered state. Previous work in our group has characterized the LLP as a supercooled liquid, with solid-like properties that resemble a soft glass. Notably, had the ordered structures found here been identified when this sample was first investigated, the discovery would have preceded identification of the σ phase 1 and DDQC 5 in diblock copolymer melts by more than

a decade. Moreover, Papadakis's 1999 study predates even the first reports of σ^{44} and DDQC⁴⁵ packings generally across soft materials, re-emphasizing the importance of high-resolution scattering for the discovery of new micellar assemblies in soft matter.

To better resolve the phase transition temperatures, we collected DMA data at multiple frequencies while heating the material at 0.2 °C/min. As shown in Figure 3A, a sharp discontinuity in G' was observed at 132 °C, which we attribute to the ODT. This is in excellent agreement with SAXS (Figure S8) and DSC measurements (Figure S2C), the latter of which showed a small yet detectable endotherm at 133.5 °C on the first heating ramp consistent with past investigations of low molecular weight, asymmetric, particle-forming copolymers.⁴⁶ In addition to this sharp discontinuity at the ODT, we observed a smaller step discontinuity in G' at 110 °C that, as discussed below, can be attributed to the σ -BCC OOT. Unlike the ODT, the temperature associated with this transition was found to exhibit some dependence on both the temperature ramp rate and direction (i.e., heating versus cooling). As shown in Figure S9, there is finite hysteresis on heating and cooling at a 1 °C/min ramp rate, with discontinuities in G' appearing at 120 and 108 °C, respectively. However, complementary SAXS measurements (Figure S8) revealed that the persistence of the higher G' plateau on heating at 1 °C/min is a consequence of BCC-σ coexistence, which begins at 112 °C and ends at 120 °C consistent with the drop in G'. We can conclude that $T_{\rm OOT} = 110 \pm 2$ °C, where the error identifies the minimum and maximum observed values of the T_{OOT} . We note that the lack of a more significant hysteresis in the ODT and OOT-a feature commonly reported in previous studies dealing with various particle packings^{7,47,48}—reflects the rapid segment dynamics associated with the low glass transition temperatures of PEP and PDMS.

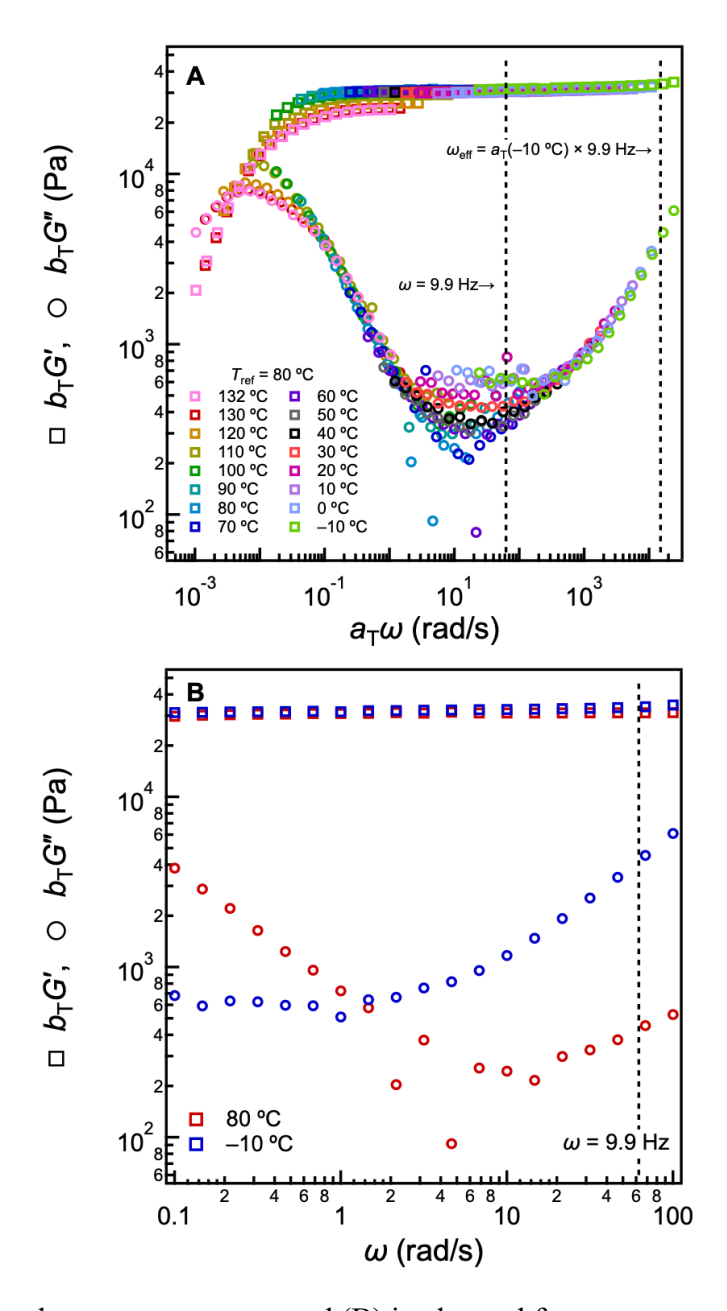


Figure 3. (A) Isochronal temperature ramp and (B) isothermal frequency sweep data collected *via* DMA while heating at 0.2 °C/min and with 1% strain amplitude. All data originates from the same set of frequency sweep measurements collected on heating. The data were separated by frequency to produce the plot in (A) and shifted in frequency by a factor a_T *via* time-temperature superposition (TTS) to produce the plot in (B). Data in (B) were also vertically shifted by a factor $b_T = \rho(T) T / (\rho(T_r) T_r)$, where ρ is the density of the copolymer and $T_r = 80$ °C is the reference temperature. Shift factors are given in Figure S4. Although the presence of multiple ordered morphologies results in a deviation from the Williams-Landel-Ferry (WLF) temperature dependence, TTS provides a useful means of representing in one figure the phase-dependent viscoelastic response of the copolymer. Frequency sweep data over the full temperature range (-10 °C $\leq T \leq 132$ °C) can be found in Figure S10.

Linear Viscoelastic Properties. As shown in Figure 3A, the linear viscoelastic response of

PEP-PDMS is a strong function of frequency in the BCC window, impacting the magnitude of the drop at the OOT. This is particularly evident on shifting the frequency data according to the time-temperature superposition (TTS) principle and correcting for the temperature dependence of the moduli as shown in Figure 3B. Although both the BCC and σ phases yield similar solid-like behavior (*i.e.*, a plateau in G'), the superimposed data reveal two distinct frequency responses with different shifted terminal relaxation frequencies $a_T\omega_x$ and plateau moduli G_N as shown in Figures 3B and S10. Conclusions based solely on the former, which corresponds to the crossover in the loss and storage moduli (G'' and G'), can be complicated by a known dependence of the terminal relaxation frequency ω_x on strain amplitude, temperature, and degree of order, the latter of which is impacted by annealing time. ^{49,50} In fact, the transition to a more liquid-like scaling below the ODT for $\omega < \omega_x$ can likely be attributed to the narrowness of the linear viscoelastic window at high temperatures (see Figure S3). In contrast, the observed difference in the BCC and σ phase plateau moduli ($G_N, \sigma/G_{N,BCC} \approx 1.3$) is not impacted by many of these variables.

Reports on the LVE properties of the σ phase in relation to the BCC phase are limited due in part to complications stemming from the often slow ordering kinetics of the σ phase, ⁴⁸ but other authors have observed a similar difference in the σ and BCC plateau moduli, ^{5,47} suggesting an increase in G_N is a signature of σ phase formation. Simulations of optimal foams, wherein the elasticity of the minimal froth Voronoi partition approximates the mechanics of our deformable micellar particles, found that a Weaire-Phelan foam isostructural to the FK A15 phase has a shear modulus ~1.1 times greater than that of a Kelvin foam with BCC symmetry—a value comparable to our result. ⁵¹ Notably, this value was largely unaffected by cell volume dispersity, pointing to a packing-dependent linear elastic response. Indeed, the role of σ phase formation in the hardening of metals and alloys is well-known, ^{52–57} primarily due to the deleterious effects of σ precipitates on stainless

steels.⁵⁸ As such, we attribute the higher relative shear modulus of the σ phase observed herein to an apparent packing-dependent elasticity that extends from atomic to mesoscopic crystals.

Resolving Phase Behavior at Low Temperature. Still unexplained is Papadakis's observation of an apparent BCC phase at -20 °C under LAOS. As noted above, linear DMA revealed no evidence of a phase transition at temperatures below the σ -BCC OOT. However, SAXS results

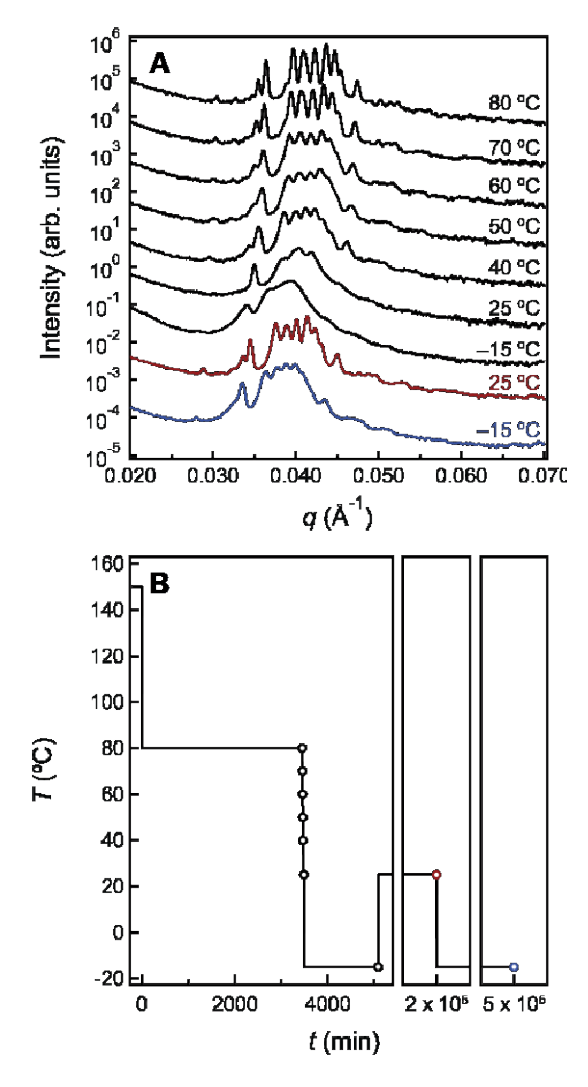


Figure 4. (A) Vertically shifted 1D scattering traces obtained on cooling a well-ordered σ phase as shown in (B) and described in the text. Circles in (B) indicate the time and temperature at which each trace in (A) was collected, where the top trace corresponds to the earliest time point. The data in red were obtained on reheating the sample to room temperature and annealing for 115 days. The blue data were obtained on subsequently re-cooling the sample to -15 °C and annealing for an additional 243 days.

were inconclusive, suggesting the system becomes kinetically trapped for $T \le 40$ °C. To overcome these kinetic limitations, we incrementally cooled a well-ordered σ phase (SAXS shown in Figures 2 and S6) from 80 °C to -15 °C, approximating a 3 °C/min cooling rate, and then annealed the sample for 27 h as detailed in Figure 4B. As shown in Figure 4A, the σ phase was initially retained when cooled to 40 °C but appeared to transition into a DDQC at 25 °C. On cooling further to -15 °C, we observed substantial disruption of the scattering pattern coincident with a shifting of the SAXS peaks to lower q. This shift corresponds to a 7% increase in the mean particle radius $\langle R \rangle \approx \langle R \rangle_{\sigma} = 2\pi^{2/3}/(5^{1/3}(c/a)^{2/3}q_{002})$ and a 33% increase in the mean aggregation number $\langle N_{agg} \rangle = 4\pi \langle R \rangle^3 \rho N_{av}/(3M_n)$, where c and a are lattice parameters ($c/a \approx 0.53$), $M_n = 12,500$ g/mol is the copolymer molecular weight, ρ is the copolymer density, and N_{av} is the Avogadro constant (see Supporting Information for additional details). An increase in N_{agg} is anticipated on cooling as the system attempts to minimize the interfacial area per chain, but it was unclear whether the observed loss of translational order and peak smearing was due to the change in N_{agg} , which could result in structural disruption, or an incomplete phase transition.

To resolve this issue, we reheated the sample to room temperature (T = 25 °C) and annealed it for 115 days. As shown in Figure 4A, a well-resolved σ phase is recovered. Subsequently cooling the sample to -15 °C and annealing for an additional 243 days similarly retains the σ phase, albeit with a larger unit cell and some degree of peak broadening indicative of reduced grain sizes (Figure 4A). This provides compelling evidence that σ is the equilibrium packing for $T \le 110$ °C and that the structural distortions observed on cooling most likely stemmed from a changing $N_{\rm agg}$. In more detail, conservation of mass requires a reduction in the micelle number density to increase $N_{\rm agg}$. This requires either the fusion of adjacent micelles and subsequent mass redistribution via chain exchange or an Ostwald ripening process—though, the latter is less likely to dominate due to the

high energetic barriers associated with fully evaporating a micelle.⁵⁹ This process will inevitably result in the generation of lattice defects as it effectively eliminates micelles from the crystal and we suspect this is at the source of the lost order. Last, we note that these results also provide an explanation for the reduction in intensity reported by Papadakis *et al.* in optical birefringence measurements below 80 °C (Figure 1E), as significant disruption of the σ phase on cooling and the resultant reduction in the grain size would likely reduce the optical birefringence of the sample. However, other features of Papadakis's results under LAOS remain unexplained, in particular the re-entrant BCC phase.

Low Temperature Phase Behavior Under LAOS. To better rationalize past results under LAOS, we performed shear-SAXS measurements with the beam aligned parallel to the shear gradient direction ∇ as shown in Figure 5 (further details can be found in the Materials and Methods section). After loading, the sample was disordered by heating to 150 °C and then rapidly cooled (30 °C/min) to −10 °C, resulting in a broad scattering peak (Figure S11A). As shown in Figure 6A, 23.5 min of LAOS at a strain amplitude of $\gamma = 106\%$ and frequency $\omega = 9.9$ Hz (62 rad/s) resulted in a 2D scattering pattern that closely resembles the one reported by Papadakis et al. at -25 °C (Figure 6C). 41 Azimuthal integration of the 2D pattern (Figure 6B) reveals 4 scattering reflections $(q/q^* = 1, \sqrt{2}, \sqrt{3}, \sqrt{4})$ consistent with the $Im\overline{3}m$ space group symmetry of the BCC phase. Further confirming this phase assignment, plots of the intensity at q_{110} as a function of azimuthal angle (Figure 6E) show a roughly 6-fold symmetry in the principal scattering reflection that, as shown in Figure 6A, can be indexed to the reciprocal lattices of a twinned BCC structure with the (110) plane oriented perpendicular to the incident beam (Figure 6F) consistent with past work. 41,60,61 We note that a scattering reflection is anticipated in the purple shaded region of Figure 6E, but this fell outside the range captured by the detector. Further, given the lack of unique higher order scattering reflections, the (110) reflections intersected by the purple (110) reciprocal lattice in Figure 6A could reflect either an additional (110) grain or a (211) grain, the latter of which has been observed previously at a similar 90° angle from the direction of shear.⁶¹ Nonetheless, we believe that the sample was predominantly oriented with the BCC [110] direction parallel to the incident beam as Papadakis *et al.* observed only 2-fold symmetry (Figure 6D) with no evidence for a (211) reflection on rotating a nearly identical structure at –25 °C by 29° about the *x*-axis of the sample (see Figure 5).⁴¹ This agrees well with simulated diffraction patterns shown in Figure S12. Importantly, attempts at indexing the pattern in Figure 6A to various FK phases and close-packed structures were unsuccessful, leaving us confident in this phase assignment.

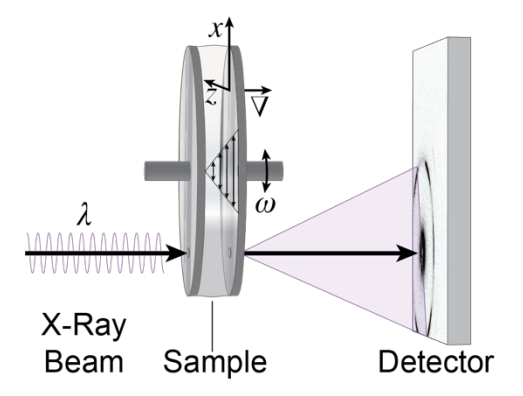


Figure 5. Shear-SAXS sample orientation relative to the incident synchrotron X-ray beam.

Although quiescent SAXS measurements indicate that the σ phase is the equilibrium packing for T < 110 °C, decisively establishing the equilibrium phase behavior far below $T_{\rm ODT}$ is complicated by asymptotically slow nucleation and growth kinetics. Self-consistent field theory (SCFT) anticipates that the σ phase should persist at equilibrium as the temperature is lowered (*i.e.*, as segregation strength increases).^{3,8} However, a re-entrant equilibrium cubic phase (BCC or A15) could potentially occur in an actual physical system due to changes in volumetric composition or conformational asymmetry over the >100 °C temperature range of the experiments. Any change in composition (*i.e.*, volume fraction of PEP) would be negligible as both blocks have

comparable thermal expansion coefficients,⁴² but we estimate that conformational asymmetry would increase from $\varepsilon = 1.6$ to 2.0 on cooling from 140 °C to –25 °C.^{42,62} Critically, both theory^{3,8} and experiment^{3,9} have found that an increase in conformational asymmetry and/or segregation strength χN , which scales inversely with temperature, should further stabilize the σ phase over the BCC phase. Further, the theoretical boundary separating the σ and A15 phase regions is predicted

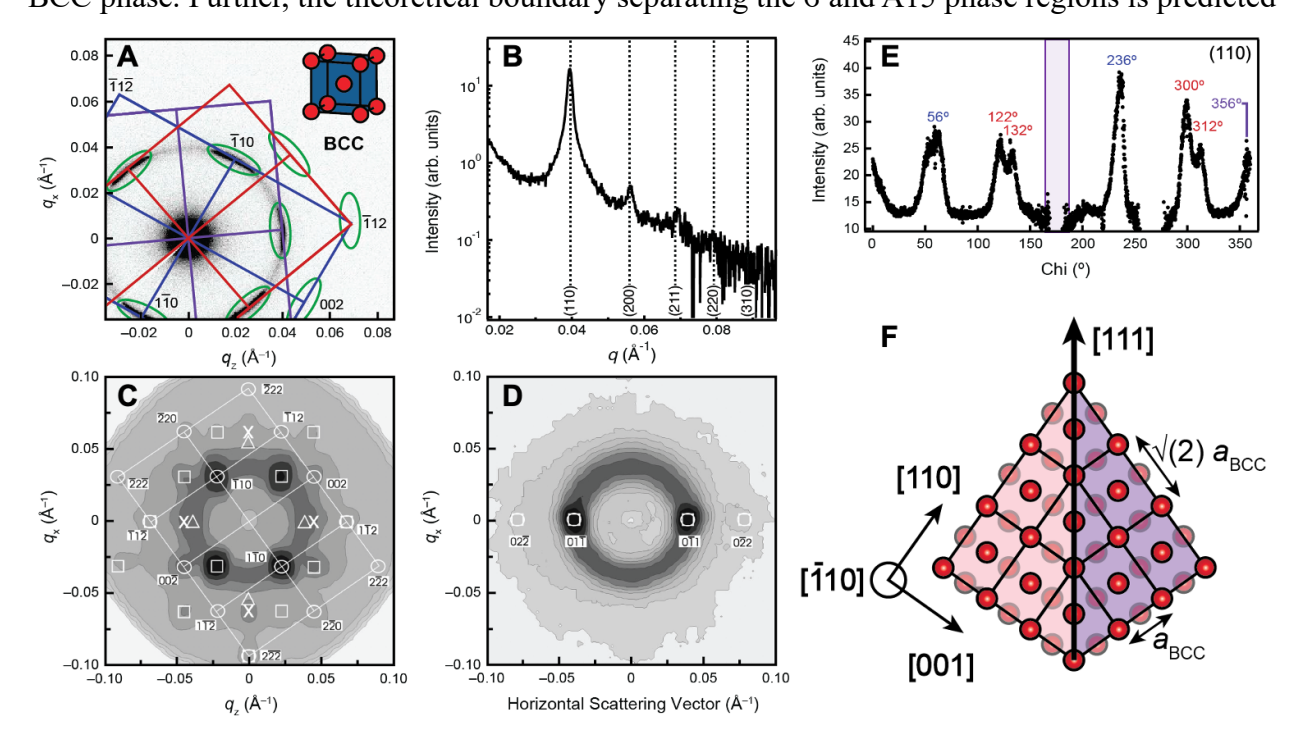


Figure 6. Scattering data collected following low temperature oscillatory shear. (A) 2D-SAXS pattern collected following 23.5 min of large amplitude oscillatory shear ($\gamma = 106.2\%$, $\omega = 9.9$ Hz) at -10 °C. Reflections are identified with green ovals and indexed to a twinned BCC structure oriented with the BCC [110] axis parallel to the incident beam. Blue, purple, and red grids denote the reciprocal lattices of (110) grains, but we note that the spots intersected by the purple grid may also correspond to a (211) grain. The pattern in (A) can be found without indexing in Figure S11D. (B) 1D-SAXS data obtained via azimuthal integration of the 2D SAXS pattern in (A). (C) 2D SANS pattern collected following 102 min of large amplitude oscillatory shear ($\gamma = 100\%$, $\omega =$ 15.9 Hz) at -25 °C by Papadakis et al. where squares and circles denote the twinned BCC structure, triangles are associated with (110) reflections from an additional grain, and X indicate sites of potential multiple scattering. (D) 2D-SANS pattern collected on rotating the sample in (C) by 29° about the x-axis in Figure 2. (E) Azimuthal angle (Chi) versus intensity data obtained from (A) for the (110) scattering reflection where Chi = 0° corresponds to the center of the ($\overline{1}12$) reflection in (A), increasing in the clockwise direction. The purple shaded region in (E) was not captured by the detector. (F) Schematic illustration of a BCC twin. (C, D) Reproduced from ref. 41, with the permission of AIP Publishing.

to shift to higher f_{PEP} with decreasing temperature, also stabilizing the σ phase *versus* A15.^{3,8} Therefore, we believe, consistent with the quiescent SAXS results, that the σ phase is the equilibrium packing at low temperature and the twinned BCC structure observed under LAOS is shear-induced.

Several authors have reported on shear-induced phase transitions in colloids and block copolymer melts. The most prevalent of these is the transition from random close-packing to a face-centered cubic (FCC) or hexagonally close-packed (HCP) structure. 63,64 although shearinduced BCC-FCC⁶⁵ and sphere-cylinder transitions^{61,66} as well as shear-induced ordering⁶⁵ have also been found. Shear-induced ordering may help to explain the dramatically faster ordering kinetics we observe under shear ($t_{\text{shear}}/t_{\text{quiescent}} < 7 \times 10^{-5}$), but unexplored is why a BCC packing would be favored over the σ phase or a DDQC under LAOS. This presumably stems from differences in the shear deformation behavior of the different packings. For a BCC crystal, this behavior has been widely explored across condensed matter. 60,61,67-69 Slip occurs in the classical sense via dislocation movement in the closest packed (111) directions predominantly along {110} planes, as is evident from our results in Figure 6, but also along the {211} and {321} planes, yielding a total of 48 possible slip systems. 70 In contrast, the shear deformation behavior of soft, topologically close-packed micellar phases remains poorly understood, but a wealth of literature on these packings in metals and alloys suggests the shear deformation behavior of the FK σ and DDQC phases is much more complicated than for BCC.

Studies of β -uranium, which is characterized by a FK σ crystal structure, have revealed the existence of three slip systems: two of the type $\{110\}\langle001\rangle$ and a third in the $\{100\}$ plane and highest density $\langle001\rangle$ direction.^{57,71–73} The former is best described by Kronberg's zonal dislocation model, wherein slip in the $\langle001\rangle$ direction requires rotation of the hexagonal packing

motifs within the {110} zone of the densely-packed {001} planes (see illustration in Figure S13A); this translation is analogous to the mechanism underlying operation of a double rack and pinion device. 72 The latter, the {100}(001) slip system (see illustration in Figure S13), is activated last in β-uranium and involves a split dislocation of the Frank partial type, resulting in stacking faults in the ABACABAC... layering of the {001} planes.^{73,74} An interesting conflict in the metals and alloys literature concerns the high ductility of β-uranium in contrast to the brittleness of several alloys with the same σ crystal structure (eg., Fe-V, Fe-Cr, Co-V, Ni-V, and Nb-Al).⁷⁵ This was rationalized by Kitchingman as a consequence of the stability of uranium in any of the coordination number (CN) 12, 14, and 15 lattice sites of the σ crystal, as opposed to the preference in alloys for a particular component CN. 75 Considering Nb-Al as an example, Nb exists with CN 12, 14 and 15, but Al only exists with CN 12 and 14. As such, a slip mechanism requiring the translation of Al into a CN 15 lattice site is energetically disfavored. This also explains the prevalence of {100} stacking faults over Kronberg zonal dislocations in alloys such as Fe-Cr⁷⁴ as the {100}(001) slip system involves a shuffling of atoms through CN 12 and 14 or CN 12 and 15 lattice sites (see Figure S13B), whereas the {110}(001) slip system involves CN 12, 14, and 15 sites.

Although our system is nominally single component, the particle size distribution $(0.91 < V_{\text{micelle}}/\langle V_{\text{micelle}}\rangle < 1.07)^{76}$ necessary to fill space at constant density in a σ phase likely has an effect comparable to alloying elements with different preferred CN, particularly at shear deformation rates higher than the rate of mass equilibration. Analogous to the preference of an element for a particular CN based on its electronic configuration, a micelle will prefer lattice sites compatible with the micelle volume in order to prevent accumulation of significant lattice strain. This preferred site volume increases coincident with increasing CN in FK phases (see Figure S13), suggesting our system may exhibit a similar preference for the $\{100\}\langle 001\rangle$ slip system. However,

there still exists a ~10% volume contrast between the CN12 and CN14 sites, complicating even this mode of slip. In studying a (Cr,Ni,Al)₂Nb alloy with FK C14 crystal symmetry, Zhang et al. observed highly unusual shear deformation behavior wherein Burgers vectors deviated from and even switched slip planes in favor of preserving the local CN and the short-range configuration.⁷⁷ This represents in some respects an extreme for topologically close-packed alloys as the existence of only CN12 and CN16 lattice sites further discretizes the preferred sites for the different elements, but it is likely similar to the strong discretization of preferred lattice site volumes in our system. As such, we expect significant deviations from classical shear deformation behavior for micellar σ packings that prevent dissipation of lattice defects and bias the already delicate free energy balance² in favor of the BCC phase, wherein a multitude of well-defined slip systems affords facile dissipation of defects under shear. Further, we expect this non-classical behavior likely extends to other topologically close-packed phases with similar constraints and nonnegligible differences in micelle volume as well as quasicrystals, wherein, even absent a preference for a particular component CN, irregular dislocation movement can drive an increase in dislocation density and phason walls.^{78,79}

Epitaxial DDQC Growth. We now turn to the unusual scattering spot pattern observed on heating the shear-oriented twinned BCC specimen to 50 °C (Figure 1C). Following the 23.5 min of LAOS at –10 °C discussed in the previous section, we ceased shear and heated the sample to 50 °C at a rate of 30 °C/min. As shown in Figures 7A and S14, higher order reflections associated with the twinned BCC structure quickly disappeared in concert with a broadening of the principal scattering reflection and the development of arcs intermediate to the original (110) reflections. After 112 min, we obtained a scattering pattern very similar to that reported by Papadakis *et al.* (see Figures 1C and 7B). However, with additional annealing, the spots split in *q*, resulting in a 1D

scattering trace consistent with a DDQC (Figures 7A and S14G). This DDQC structure persists even after annealing the sample for 503 min and subsequently heating it to 80 °C. After an additional 134 min of annealing at 80 °C, we observe a significant sharpening of the scattering reflections (Figure 7C). Upon heating further to 95 °C, the σ phase begins to emerge, retaining the

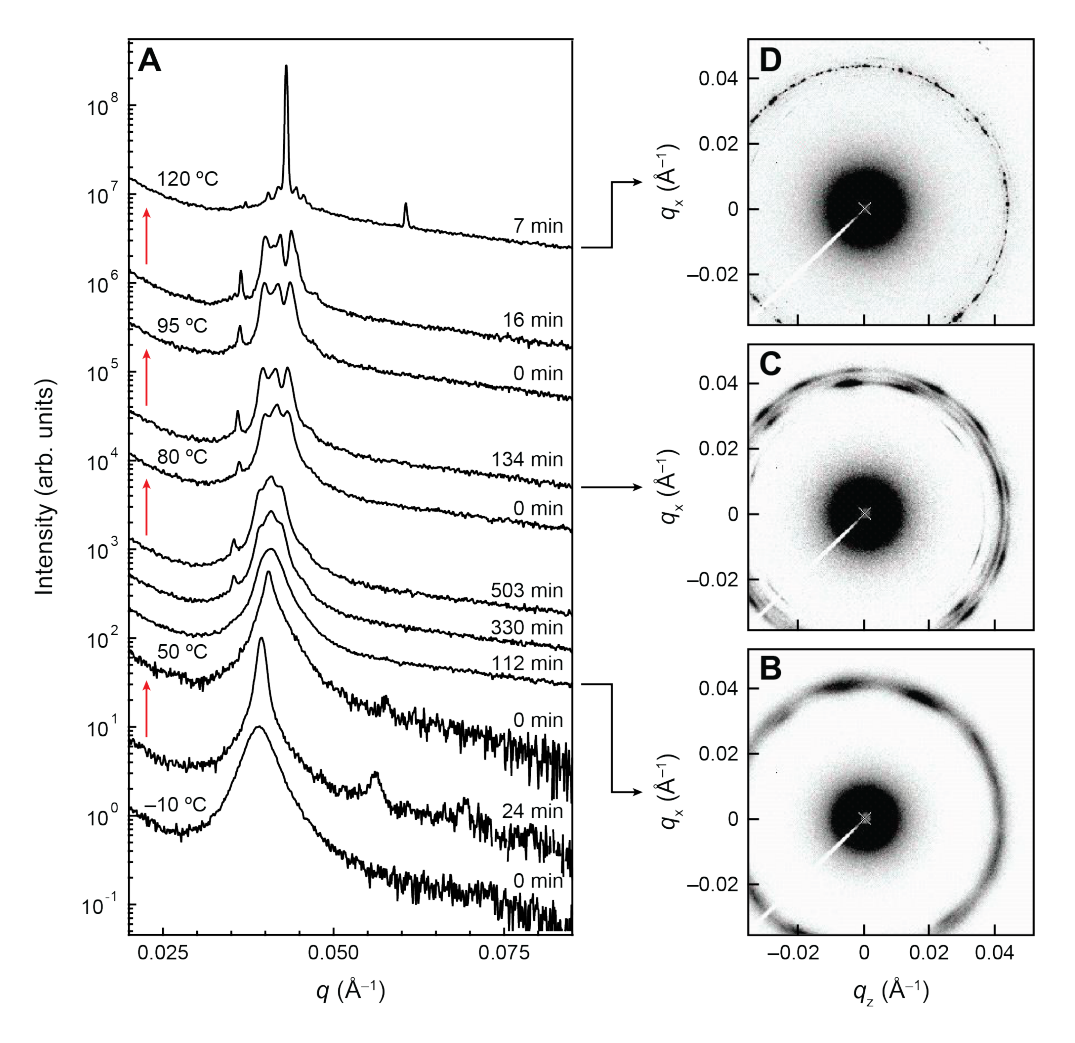


Figure 7. Scattering data collected on heating the shear-oriented BCC phase in Figure 6. (A) 1D scattering profiles were collected on shear-orienting the sample at −10 °C for 24 min and heating stepwise without shear. Time 0 on the right of (A) corresponds to the time at which the sample reached each temperature (denoted on the left). After cessation of shear, the sample was annealed at 50, 80, 95, and 120 °C for 503, 134, 16, and 7 min, respectively, using a 30 °C/min heating rate at each temperature step (denoted by red arrows in A). 2D scattering patterns on the right were collected at (B) 50, (C) 80, and (D) 120 °C after annealing for 112, 134, and 7 min, respectively, at each temperature. Additional scattering patterns collected at 50 °C can be found in Figure S14.

anisotropy of the DDQC (Figure 7A), but, on heating through the σ-BCC OOT and annealing at 120 °C for 7 min, a largely isotropic BCC phase forms (Figure 7D).

These results raise several interesting questions. First, the anisotropic 2D scattering patterns obtained from the DDQC in Figures 7 and S14 stand in stark contrast to the almost universally isotropic DDQC patterns obtained without shear orientation (Figure S15). Does this anisotropy point to a BCC-DDQC epitaxy and, if so, how might the transformation proceed? Second, this anisotropic DDQC state persisted cumulatively for more than 630 min at 50 and 80 °C, but a well-resolved σ phase emerges in less than 100 min on cooling a BCC phase to 80 °C (Figure S18E). What is driving the dramatic slowdown in the ordering kinetics observed for a BCC-DDQC-σ ordering pathway on heating *versus* a BCC-σ path on cooling and why do we see a DDQC intermediate? Last, the anisotropy of the DDQC phase was lost on heating through the σ-BCC OOT but anisotropic BCC phase on heating the anisotropic DDQC through the σ-BCC OOT but anisotropic DDQC growth on heating an anisotropic BCC phase? We will first focus on the question of BCC-DDQC epitaxy and address the latter questions in the following section.

The first identification of a DDQC in soft matter relied on spot patterns obtained from micro-diffraction of a dendrimer slowly cooled in a capillary,⁴⁵ but subsequent reports on the orientation of quasicrystals and even FK phases in soft matter are rare. Peterca *et al.* obtained an oriented FK A15 phase on heating an extruded hexagonally packed cylinder (HEX_C) phase in a thermotropic liquid crystal⁸⁰ and Fischer *et al.* discovered colloidal quasicrystals with 12- and 18-fold diffraction symmetry on cooling a shear-oriented FCC phase with its [111] axis aligned parallel to the incident beam.⁸¹ Although we are unaware of any reports of BCC-DDQC epitaxy in soft matter, there are well-known epitaxies between the (111), (10), and (110) planes of the FCC, HEX_C, and BCC phases, respectively.^{61,82} Similarities in the local packing of FK and QC packings, which can all

be assembled from closely related tetrahedrally close-packed micellar clusters, suggest that analogous epitaxial relationships may hold here.⁸³

As shown in Figure S14, the orientation of the DDQC is clearly templated by the preceding twinned BCC structure. This is evident in the unusual anisotropy of the DDQC scattering pattern, but also in the essentially identical orientation of the BCC (110) and DDQC (12100) and (12101) scattering reflections. This points to an epitaxial BCC-DDQC phase transition, yet the orientation of the resultant DDQC relative to the twinned BCC phase remains unclear. As shown in Figure 7C, greater than 2-fold rotational symmetry at q_{00002} suggests the existence of multiple DDQC grains. 45 Moreover, the presence of a (00002) scattering reflection coupled with greater than 2-fold and 4-fold symmetry in the (12100) and (12101) reflections, respectively, indicate that the DDQC was not oriented with the 12- or 2-fold axes parallel to the incident beam; calculated diffraction patterns can be found in Figures S16. The presence of multiple DDQC grains with 12-fold axes oriented off the incident beam direction significantly complicates a full indexing of the pattern in Figure 7C. However, scattering patterns collected by Papadakis et al. following a similar experimental protocol are seemingly less complicated (Figure 1C).⁴¹ We attribute this to three factors: a longer annealing time in the previous work (11 h), a better oriented twinned BCC structure, and poorer scattering resolution, which may lead to some peak overlap and an absence of less intense reflections. Nonetheless, a key advantage of SANS was that it enabled rotation of the sample stage about the x-axis (Figure 5). Notably, the 10-spot pattern in Figure 1C was recovered in 60° intervals of x-axis rotation, an 8-spot pattern emerged at intermediate 30° angles, and a 2-spot pattern was recorded at all other angles. 41 A full indexing should be able to account for all of these scattering patterns. However, again, we find none of these patterns to be consistent with orientation of the 12-fold axis parallel or perpendicular to the incident beam (Figure S16) and so we turn to a comparison of the BCC and DDQC structures.

Unlike its periodic approximants, a DDQC is aperiodic in two dimensions with a 12-fold rotational symmetry in the aperiodic plane, making it best described *via* a 5-dimensional indexing scheme (Figure 8A). This lack of translational symmetry about the 12-fold axis is incommensurate with the periodicity of the BCC (110) plane, complicating the apparent epitaxial relationship. Nonetheless, there are clear structural relationships between the two phases. Analogous to its

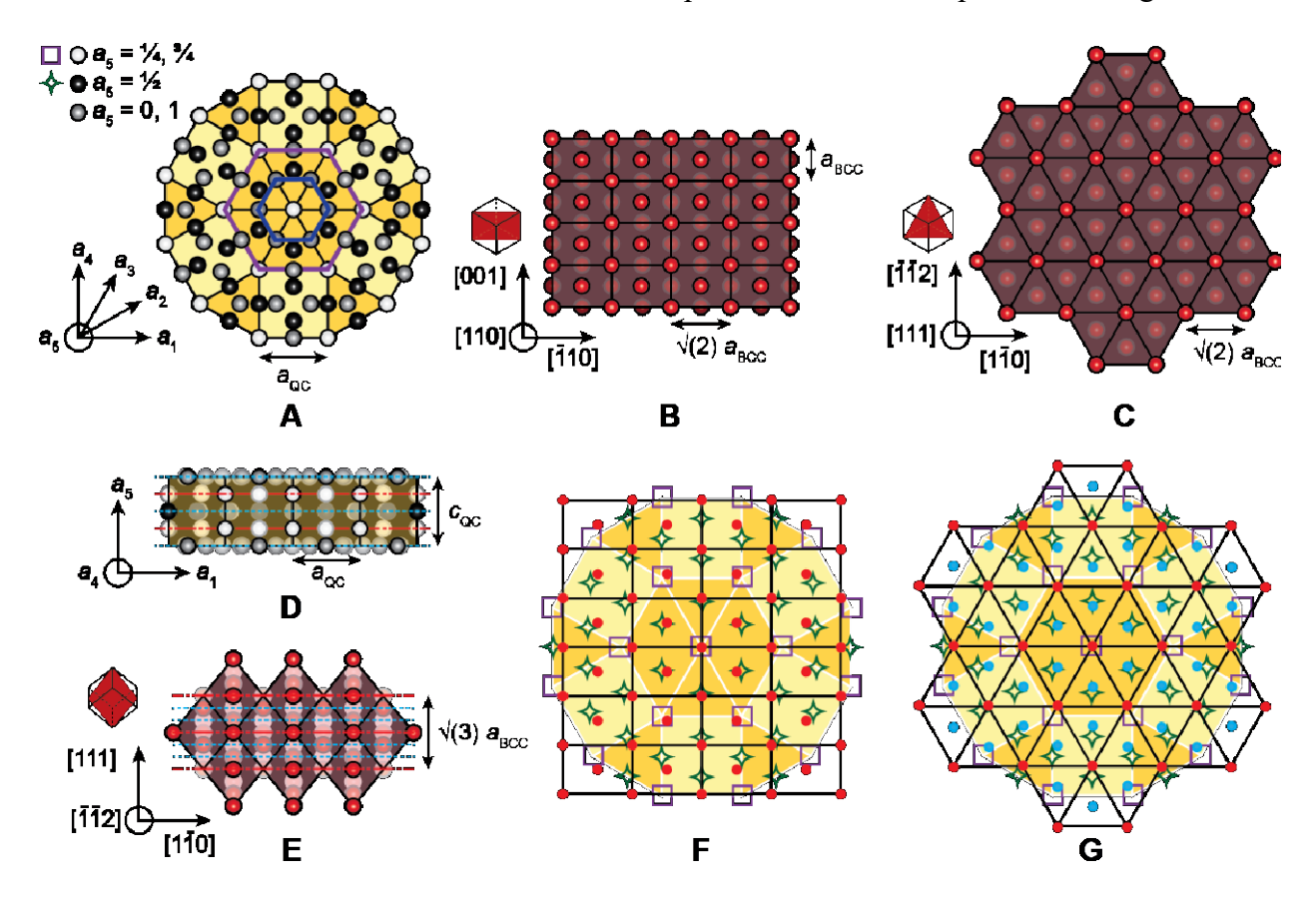


Figure 8. Schematic illustrations of the packings (A) parallel and (D) perpendicular to the 12-fold DDQC axis and in the (B) (110), (C) (111) and (E) ($\overline{112}$) BCC planes. Coincidence site lattice models for the 12-fold DDQC plane and the BCC (110) and (111) planes are shown in F and G, respectively. Red circles in F and G correspond to micelles within each respective BCC plane, whereas puckered green diamonds and purple squares correspond to the location of micelles within the dense and sparse planes of the DDQC. Blue circles in G correspond to the packing in subsequent BCC (111) planes denoted by blue dotted lines in E. The plane orientations relative to the BCC cubic unit cell are provided on the left in (B,C,E).

periodic approximants, a DDQC can be constructed from a 2D tiling of squares and equilateral triangles with edge length $a_{\rm QC}$ as shown in Figure 8A. Ideally, these tilings follow a Schlottman or Stampfli inflation rule. However, TEM and AFM investigations of soft DDQCs suggest the tiling is more random than anticipated by a rigorous interpretation of these rules. However, Temperature of these rules are organized periodically into alternating sparsely and densely packed layers of the type ABACABAC... and spaced a distance $c_{\rm QC}/4$ apart, where $c_{\rm QC} \approx 1.02~a_{\rm QC}$ corresponds to the periodicity along the 12-fold rotational axis ($a_{\rm S}$). In the sparsely packed planes ($a_{\rm S,A} = \frac{1}{4}, \frac{3}{4}$), micelles are positioned at the vertices of the 2D tiling. In contrast, the two densely packed planes ($a_{\rm S,B} = 0$, 1 and $a_{\rm S,C} = \frac{1}{2}$,) are offset by 30° and characterized by a pseudohexagonal packing sometimes referred to as the Kagomé net with a smaller intermicellar spacing of $\sqrt{(3)/3}~a_{\rm QC}$ (0.58 $a_{\rm QC}$; see Supporting Information).

Similar intermicellar spacings and pseudohexagonal packing motifs can be found in the (110) and (111) planes of the BCC packing. This is evident in Figure 8 wherein the DDQC and BCC packings are drawn to scale, reflecting the roughly constant mean particle radius calculated from SAXS data before and after the phase transition ($\langle R \rangle = 10.7 \pm 0.1$ nm, see Supporting Information for calculation details). To further highlight these structural relationships, we constructed coincidence site lattice models through superimposition of the particle packing in a densely and sparsely packed 12-fold DDQC plane with the (110) and (111) planes of the BCC phase. We note this approach is analogous to that used in rationalizing the epitaxial growth of decagonal and icosahedral quasicrystals on single crystal BCC substrates in metals alloys. As shown in Figures 8F and G, the packings display excellent agreement in projection. In both cases, the error in the intermicellar spacing for both the sparse and dense planes is less than 11% (see Supporting Information). However, we note that adoption of a DDQC packing with the 12-fold axis oriented

parallel to the BCC [110] axis would require the creation of a new plane *via* translation of micelles coincident with the position of squares associated with the sparse plane in the BCC [110] direction by a distance $c_{QC}/4$. This distance is comparable to the half-spacing between (110) planes $(a_{BCC}\sqrt{2}/4) = 0.88 \ (c_{QC}/4)$, making this plausible. But, to produce the patterns in Figure 7, this lattice translation would also need to somehow drive a tilting of the 12-fold DDQC plane.

In contrast, the packing in the (111) plane (red circles in Figure 8G) is nearly identical to that of the sparse plane (squares in Figure 8G) within the 3⁶ tiling (6 triangles meeting at a point) central to the dodecagonal cogwheel shown in Figure 8A, and repeats in the [111] direction at a distance comparable to the spacing between sparsely packed planes ($c_{OC}/2$) = 0.93 ($\sqrt{3}/2$ a_{BCC}) (indicated by red lines in Figures 8D and E). Moreover, the combined packing of the intermediate planes located at $d_{[111]} = \sqrt{3}/6$ a_{BCC} and $\sqrt{3}/3$ a_{BCC} (denoted by blue lines and circles in Figures 8E and G) is nearly coincident with the packing of the first set of dense DDQC planes (marked by blue lines in Figure 8D for comparison), which occur at $c_{OC}/4 \approx \sqrt{(3)/4} \, a_{BCC}$. Although subsequent layers would require a 30° rotation to adopt the packing of the subsequent dense DDQC plane, we speculate that a BCC-DDQC phase transition could occur through fairly modest rearrangement of the (111) plane. Further, this would result in a 35.3° tilt of the aperiodic plane normal away from the BCC [110] axis (see Figure S17) in at least qualitative agreement with the observed off-axis DDQC alignment. A more complete understanding of this epitaxial transformation will require acquisition of scattering data with rotation of the shear-oriented specimen relative to an incident X-ray or neutron beam, along with more involved crystallographic computations beyond the scope of the current work. We note that the role played by grain boundaries in the twinned BCC structure is also unclear and that these boundaries may impact nucleation of the growing DDQC. Regardless,

the relationships described here provide a plausible explanation for the observed BCC-DDQC epitaxy.

Temperature-Dependent Epitaxial Growth and Shear-Induced Disorder. As discussed above, heating the anisotropic DDQC above the OOT to 120 °C leads to an isotropic BCC phase (Figure 7D). This finding could point to an irreversibility in the epitaxial relationship. However, on cooling a shear-oriented BCC phase from 120 °C to 80 °C (Figure S18E), we obtain a similarly unoriented FK σ phase, suggesting a lack of epitaxy on cooling through the OOT as well. This could be due to a temperature dependence in the ordering dynamics. As will be discussed below, we suspect mass exchange plays a larger role in the ordering process at high temperature than cooperative micelle rearrangements, but this loss of anisotropy could also be due to the lack of an intermediate DDQC state near the ODT. However, the DDQC and FK σ packings are very closely related, with the σ (001) plane constructed from the same 4.3.4.3² tiling that makes up >80% of the tiling in the 12-fold DDQC plane (see Figure S19).90 In fact, Kitchingman explained the martensitic BCC-σ transformation observed in metal alloys by a similar rearrangement of the BCC (111) plane (Figure 8), 75 suggesting the absence of an intermediate DDQC state is likely not the cause of the lost orientational memory. We note that the orientation of the BCC phase captured in Figure S18E at 120 °C differed from the twinned (110) orientation obtained at lower temperature (Figure 6A) as reflected in a 4-fold symmetry at q_{110} . This pattern can be indexed to a (100) reciprocal lattice as shown in Figure S18E similar to scattering patterns collected by Hamley and coworkers on shearing a BCC phase at low strain amplitudes. 91 This orientation would impact the orientation of any subsequent DDQC or σ phase, but it should not have any bearing on the above discussion.

After obtaining the well-ordered, isotropic σ phase evidenced in Figure S18D, we subjected the sample to further LAOS at a constant temperature (T = 80 °C) and angular frequency ($\omega = 9.9$ Hz) but an increasing strain amplitude ($\gamma = 35\%$, 71%, 107%, and 177%) imposed sequentially in 2

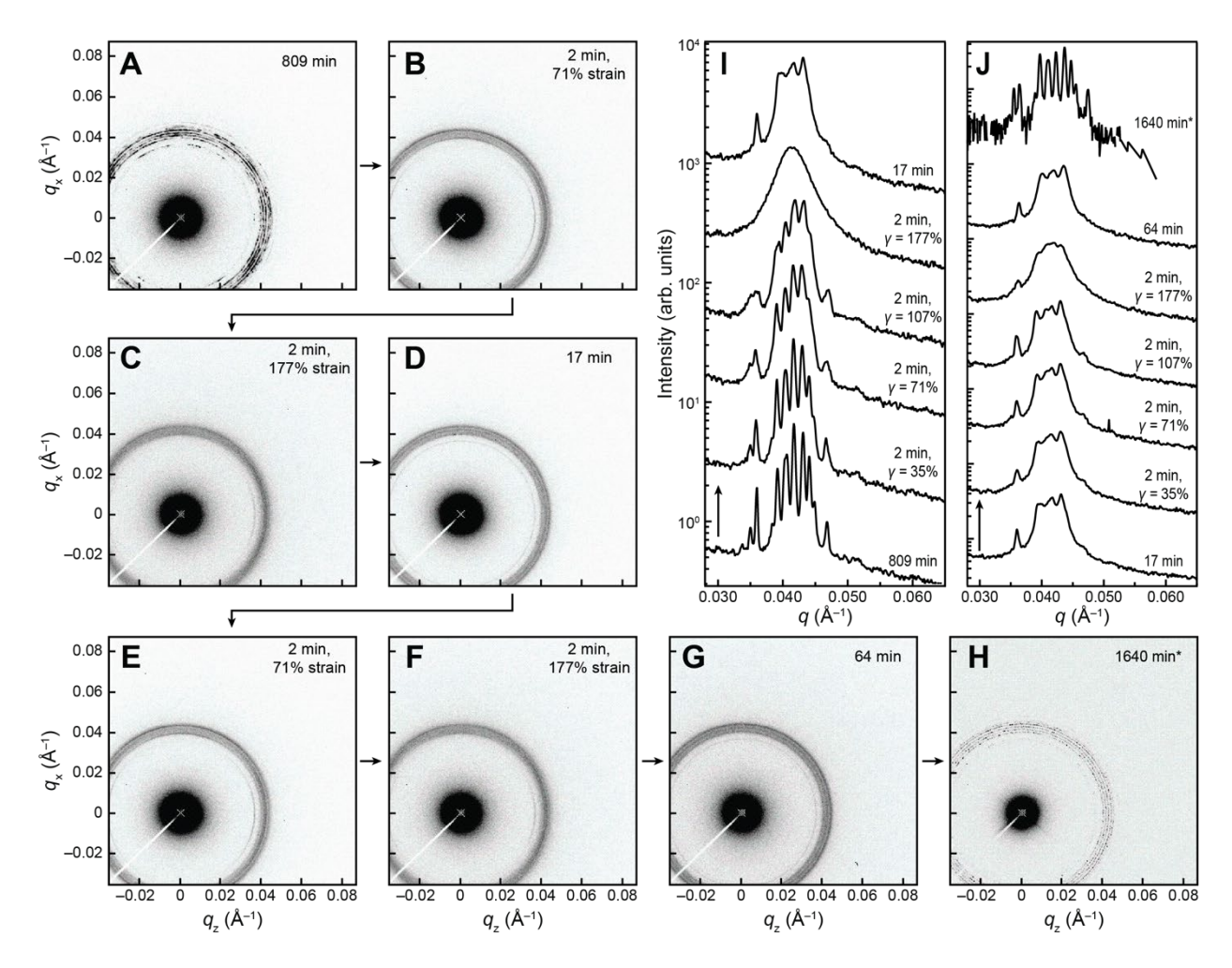


Figure 9. Scattering data obtained on shearing (A-D, I) a well-ordered σ phase and then (D-G, J) a QC at ω = 9.9 Hz. Data in (I) and (J) were vertically shifted for clarity. The σ scattering pattern in (A) and trace at the bottom of (I) were collected on cooling a shear-oriented BCC phase from 120 °C to 80 °C and annealing for 809 min as outlined in the text and Figure S18. The sample was then subjected sequentially to increasing strain amplitude in 2 min increments resulting in the 2D scattering patterns (B,C) and associated 1D traces (I). Shear was subsequently stopped and the sample was left to equilibrate for 17 min, resulting in the predominantly DDQC scattering pattern in (D) and the 1D trace at the top of panel (I) and reproduced at the bottom of panel (J). This procedure was then repeated, where scattering data collected with increasing strain amplitude can be found in (E,F,J) and in (G,J) on re-equilibration. Following shear experiments, a small amount of sample was removed from the shear cell and annealed at 80 °C for 1640 min, recovering the σ phase as shown in H & J. Arrows denote the order in which scattering patterns were collected.

min intervals. Note that this experiment is analogous to incrementally increasing the strain rate $\dot{\gamma}$, but, because the strain rate is not constant for an oscillatory measurement $(\dot{\gamma}(t) = d\gamma(t)/dt = d[\gamma(t)/dt])$ $\sin(\omega t)/dt = \gamma \omega \cos(\omega t)$, we report here the strain (or shear) rate amplitude $|\dot{\gamma}|$ calculated as $|\dot{\gamma}| = 1$ $\omega \gamma = 3.5, 7.0, 10.6, 17.5$ Hz. As shown in Figure 9I, we observed a gradual disordering of the σ phase, culminating at $\gamma = 177\%$ ($|\dot{\gamma}| = 17.5$ Hz) in a broad isotropic reflection at $q^* = 0.0414$ Å⁻¹ with a very faint (002) shoulder (Figure 9C and I). Intriguingly, after cessation of shear, the LLP state evolved rapidly into an isotropic DDQC, bearing only weak signatures of the preceding σ phase (t < 17 min; Figure 9D and I). Curiously, this intermediate DDQC state was notably absent on cooling the high temperature BCC phase (Figure S18). We subsequently performed the same shearing experiment with the predominantly DDQC packing ($\omega = 9.9$ Hz; $\gamma = 35\%$, 71%, 107%, and 177%). As shown in Figure 9J, we observed a similar disruption of the scattering pattern at high strain amplitude, but less so than was observed for the σ phase, suggesting the predominantly DDQC packing is less susceptible to shear-disruption. Further, at intermediate strain amplitudes, we observe some splitting of peaks consistent with a growing σ phase, which may be evidence that modest shear speeds up the σ ordering process. Nonetheless, we saw a similar isotropy in the 2D scattering patterns after stopping shear. Again, a well-defined DDQC rapidly reemerged with limited evidence for σ coexistence, but the transition to a well-ordered σ phase was not recorded even after annealing for an extended period of time (t > 64 min; see Figure 9G). This persistent DDQC and stunted σ growth stands in stark contrast to the relatively facile BCC-σ transition observed on cooling, wherein evidence for a well-resolved σ phase coexistence can be seen within minutes (Figure S18). In order to ensure that the persistent DDQC was not a result of sample degradation, a small amount of the sample was removed from the shear cell and annealed at 80 °C for 1640 min. As shown in Figure 9H, a well-resolved σ phase was recovered.

We summarize our results under LAOS in Figure 10. Three features stand out that have yet to be explored: (1) the very different response to LAOS at 80 °C and -10 °C despite similar experimental protocols; (2) the emergence of a DDQC following LAOS; and, as mentioned above, (3) the apparent lack of epitaxial growth on passing through the OOT. With respect to the first point, the LAOS response is impacted by the preceding ordered state, the strain amplitude, and the relative angular frequency. Clearly, the initial states of particle packing differed at -10 °C and 80 °C. However, both temperatures fall within the equilibrium σ window and, as discussed above, the σ phase gives way to a predominantly LLP at high strain amplitudes. Presumably the structure of

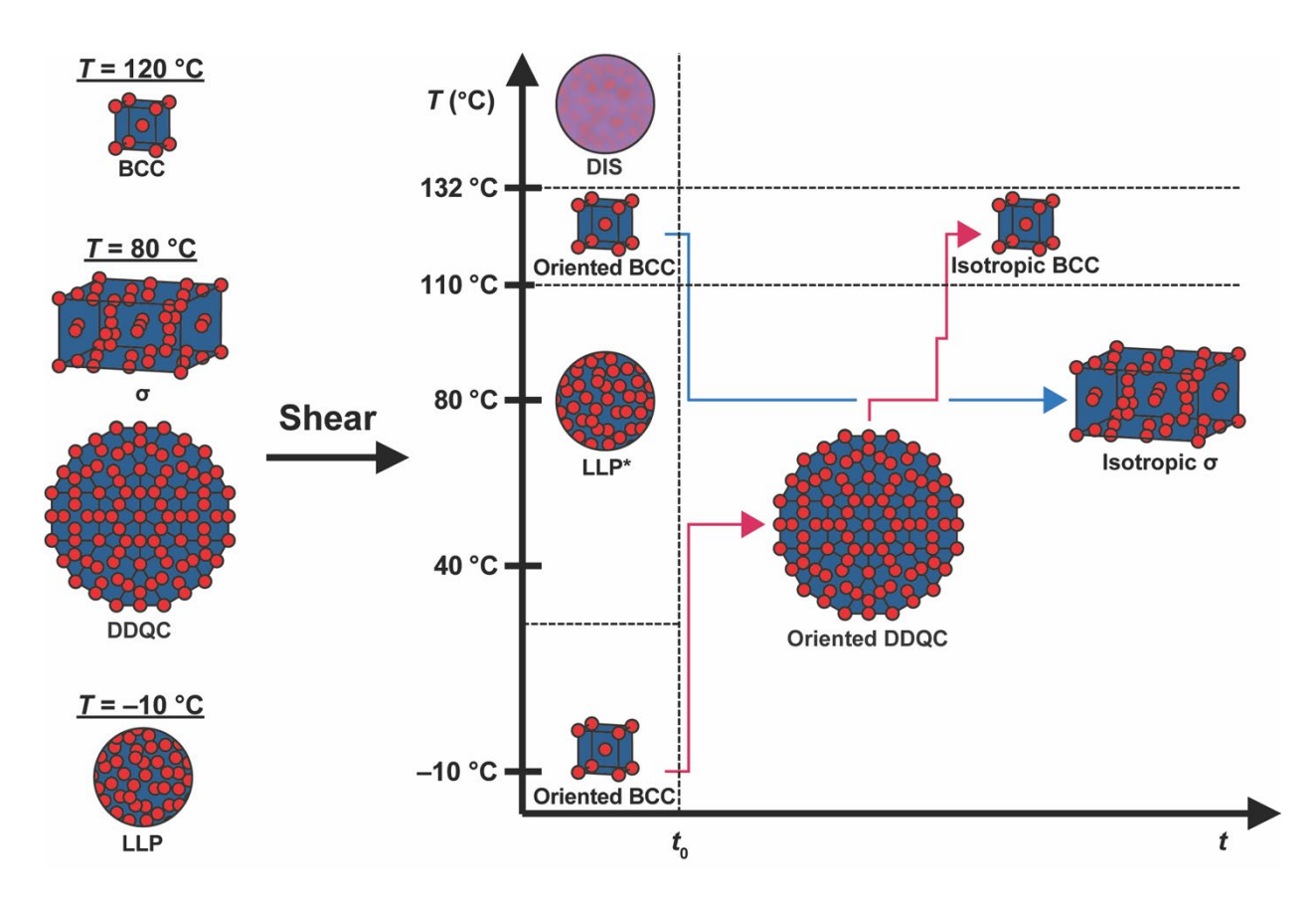


Figure 10. Schematic illustration of our results under LAOS at $\omega = 9.9$ Hz and $\gamma = 106-177\%$. The packings subjected to shear are shown on the left. Shear was stopped at a time (t_0), after which the sample was allowed to equilibrate on heating (red line) or cooling (blue line). For clarity, we omit the detailed results on re-equilibration of the LLP at 80 °C, which predominantly yielded an isotropic DDQC. Further, we note that the LLP state denoted by a star is more structured than a typical LLP and likely retains remnants of the preceding σ and DDQC states as discussed in the text.

this LLP is similar to the LLP that occurs at low temperature, both representing a globally disordered micellar packing characterized by a broad particle size distribution. However, we note that the faint (002) reflection in Figure 9C suggests the LLP state obtained under shear at 80 °C is more structured than the LLP state obtained on quenching to -10 °C from disorder. An equally likely source of the discrepancy is the shear conditions. Experiments were conducted under identical LAOS conditions, but due to the temperature dependence of the viscoelastic response, a given strain amplitude and frequency will probe a different dynamic regime on cooling as highlighted in Figure S20 for $\gamma = 1\%$. As such, the effective strain rate (*i.e.*, relative to the system relaxation time) was much greater at -10 °C than at 80 °C.

In studying BCC-forming poly(ethylene-alt-propylene)-block-poly(ethylethylene) (PEP-PEE) diblock copolymer melts under LAOS, Koppi et al. found the shear deformation mechanism to exhibit a strong dependence on the strain rate.⁶¹ At rates much smaller than the inverse defect relaxation time $\dot{\gamma}^*$ (i.e., the time to accommodate defect motion), shear resulted in structural orientation via a posited creeping deformation mechanism wherein, analogous to plastic deformation in metals, dislocation movement occurs preferentially along high particle density directions and planes. However, on increasing the strain rate such that $|\dot{\gamma}| \approx \dot{\gamma}^*$, Koppi et al. reported a disordering of the BCC lattice, evidenced by the growth of a broad isotropic scattering reflection and a significant drop in G'. This was suspected to be a consequence of an imbalance in the rates at which defects were generated and annihilated, but, importantly, the preceding twinned BCC structure reemerged on cessation of shear, suggesting BCC planes maintained the local structure and orientation in spite of the lost long-range order. Last, for $|\dot{\gamma}| \gg \dot{\gamma}^*$, the authors observed the aforementioned shear-induced phase transition from spheres to cylinders. In this limit, the rate of deformation presumably exceeds the rate of defect generation, resulting, as argued by Koppi et al.,

in affine deformation. Under an affine deformation, the lattice remains intact, but particles are severely deformed driving the shear-induced phase transition to cylinders.

Based on these arguments, we rationalize the discrepancy between the LAOS response at -10°C and 80 °C to be largely a consequence of the different effective strain rates. At 80 °C, $|\dot{\gamma}|_{max}$ = 17.5 Hz $\approx \dot{\gamma}^*_{\sigma}$ resulting in an increase in the defect density manifested by a loss of long-range order and resultant broad, isotropic scattering reflection. In contrast, at -10 °C, the higher effective strain rate exceeds the defect relaxation time of the DDQC or FK σ phase resulting in the emergence of a twinned BCC phase. Based on the observed shear orientation of the BCC phase at -10 °C, we can conclude that it exhibits a shorter characteristic defect relaxation time. The explanation for this is two-fold. First, the σ phase unit cell is much larger and more complex than the BCC phase; the σ phase has 30 particles per unit cell, each adopting one of 5 distinct geometries and volumes, as compared to the BCC phase wherein there are only 2 particles per unit cell, both of which adopt a single particle volume and geometry. Hence, a greater degree of long-range order is necessary to produce σ Bragg reflections; this may also explain the incomplete "disordering" of a DDQC under the same conditions. Second, as described above, the shear deformation behavior of the σ phase is highly unusual, with few well-defined mechanisms whereby defects can be accommodated without disrupting the structure. In contrast, the high symmetry BCC phase affords ready elimination of defects by dislocation movement along a multitude of slip systems, thus making it more favorable at high strain rates. Nonetheless, future investigations of these phases would benefit from a more extended variation of the strain rate, particularly in the limit $|\dot{\gamma}| \ll \dot{\gamma}^*$ where a creep deformation mechanism may allow for structural orientation.

The second feature that stands out in Figure 9 is the emergence of a DDQC after disordering the σ phase *via* LAOS. Mueller *et al.* recently reported a similar DDQC formation following the

crystallization-induced disordering of the σ phase. 15 Analogous to our work, the authors did not observe an intermediate DDQC on cooling from the BCC phase and rationalized the disparate σ ordering pathways as a manifestation of Ostwald's step rule, positing that nucleation of a DDQC from a LLP precedes ordering of the equilibrium σ phase because it more closely approximates the broader particle size distribution of the LLP. This might explain our results. However, unlike the complete disordering anticipated on crystallization and melting, we suspect the shear-induced disordering reported herein is likely more analogous to the disruption of long-range order observed on significant undercooling, wherein the local structural orientation is likely retained and the lost translational order stems from an increased defect density (see above discussion). Koppi et al. made a similar argument, suggesting that the "disordering" observed under LAOS at $|\dot{\gamma}| \gg \dot{\gamma}^*$ occurs due to an increase in the number of defects rather than a large-scale disruption of the packing and particle size distribution. ⁶¹ As noted above, slip is more complicated for the σ phase than the BCC phase studied by Koppi et al., but the preference for preservation of the local coordination environment that stems from the unfavorable lattice strain generated on translating micelles into positions unable to accommodate their volume suggests that the local packing will also be retained. This raises the question: Why do we observe an intermediate DDQC on reequilibration following shear deformation? The answer likely lies in the fact that the DDQC structure is very closely related to that of the σ phase, representing a largely random arrangement of same building blocks that comprise the local 4.3.4.3² σ phase tiling motif–particularly in the highly polycrystalline DDQC shown evidenced in Figure 9G. Indeed, dodecagonal cogwheel tilings have been observed via transmission electron microscopy (TEM) in heavily faulted Fe-Cr σ phases along (110) faults. 92 Therefore, we anticipate a highly disrupted σ lattice is closer

structurally to the DDQC packing than the preceding σ phase, explaining its emergence after LAOS.

Lastly, we turn to the temperature dependence of the transition from a BCC phase to topological close packing. As noted previously, we do not find any evidence of an epitaxial relationship on heating or cooling through the σ-BCC OOT, despite clear BCC-DDQC epitaxy at low temperature, and do not believe this lack of epitaxy can be attributed to the direct BCC-σ phase transition observed near the OOT (see above). However, the difference in the preferred transition pathway at low (BCC \rightarrow DDQC $\rightarrow\sigma$) versus high (BCC $\rightarrow\sigma$) temperatures does point to a temperature dependence in the ordering mechanism. This is further supported by the immense retardation in the ordering kinetics found on cooling; near the ODT, a BCC phase can be seen within a minute, but, below room temperature, ordering of the σ phase takes > 1 yr. Several authors have reported a similar slowing in the ordering kinetics, 5,19,93,94 largely rationalized as a consequence of arrested chain exchange below the ergodicity temperature $T_{\rm erg}$. Below $T_{\rm erg}$, the supercooled disordered state transitions to a non-ergodic LLP analogous to a particle-based glass. An in-depth discussion of the dynamics of our system will be presented in a future report, but we suspect a dynamic transition near $T_{\rm erg}$ can also explain the temperature dependence of the σ ordering pathway. In the limit of no mass exchange $(T < T_{erg})$, the system should be largely constrained to a martensitic, micelle translation-based ordering mechanism, wherein collective particle-level structural rearrangements would presumably favor an orientational memory and epitaxial growth. In the opposite limit, largescale fluctuations in $N_{\rm agg}$ facilitated by facile mass exchange could disrupt the local packing arrangement, favoring extensive structural reorganization. Accordingly, we attribute the nonepitaxial, direct BCC-σ ordering pathway observed near the OOT to a mass-exchange mediated phase transition, whereas the epitaxial, BCC-DDQC ordering pathway is believed to be largely

martensitic, preceding predominantly via local micelle rearrangement. We emphasize that the latter mechanism does not preclude mass exchange—a transition from the unimodal particle size distribution of the BCC phase to the multimodal DDQC particle size distribution is still required. Rather, we argue that, below $T_{\rm erg}$, mass exchange is suppressed and no longer dominates the ordering mechanism, increasing the role of local micelle rearrangement.

We anticipate a similar phenomenon also may be at the root of the slower DDQC $\rightarrow \sigma$ ordering kinetics in relation to the BCC $\rightarrow \sigma$ phase transition. The BCC $\rightarrow \sigma$ phase transition that occurs on cooling requires an adjustment in the particle size distribution (i.e., from the monomodal BCC phase distribution to the multimodal σ phase distribution) that is certainly mediated, at least in part, by mass exchange, whereas the DDQC $\rightarrow \sigma$ phase transition likely proceeds predominantly through a slower reorganization of the 12-fold DDQC plane owing to the comparable particle size distributions. Moreover, this apparent transition to micelle-translation mediated ordering dynamics on cooling could also offer an explanation for the preference at low temperatures for a BCC→DDQC ordering pathway over the direct BCC→σ phase transition observed at high temperature. In analogy to the way in which the preferred electronic configurations (i.e., the preferred CN) of different elements dictate structural reorganization in metallic alloys increased constraints on the ability of our micellar system to adjust N_{agg} far below T_{erg} serves to discretize the number of lattice sites a micelle with a given volume can occupy without incurring unfavorable lattice strains. This likely inhibits the large-scale structural reorganization needed to access a wellresolved σ packing, favoring the more random and therefore accommodating DDQC structure.

CONCLUSIONS

In closing, reevaluation of the PEP-PDMS diblock copolymer first studied by Papadakis *et al.* in 1999 has revealed a rich phase behavior including a DDQC and a FK σ phase that were hidden

from identification in the past largely due to insufficient q resolution in SANS measurements. ⁴¹ This finding puts an asterisk on the timeline of particle packing discoveries in block copolymers, ^{1–6,95,96} with the original work even preceding the discoveries of DDQC and σ packings in other forms of soft matter. ^{44,45} Along with revealing the previously hidden structure in the PEP-PDMS material, this extension of Papadakis *et al.*'s original study offers insights into the dynamics and linear viscoelastic properties of these morphologies over a wide temperature range. And, although more work is necessary to further elucidate the apparent dynamic transition about $T_{\rm erg}$, the BCC-DDQC epitaxy described herein provides a potential route to large scale oriented DDQCs, which may find applications in photonics ^{97,98} or lithography. ^{99,100} Last, we emphasize that there are certainly more missed opportunities hiding in the literature, underscoring the value in revisiting past work.

MATERIALS AND METHODS

Materials. The PEP-PDMS diblock copolymer used in this study is the same copolymer investigated by Papadakis *et al.*, $M_n = 12.5$ kg/mol with D = 1.08 and $f_{PEP} = 0.22$. Details regarding its synthesis and molecular characterization can be found elsewhere. A summary of the copolymer molecular characteristics is provided in Table S1. Size exclusion chromatography (SEC) was utilized to verify the condition of the polymer. Measurements were collected using tetrahydrofuran as the mobile phase on a Waters modular room temperature SEC equipped with a Waters 2410 refractive index detector. Molar mass dispersity was determined relative to polystyrene standards to be D = 1.1 and the trace, shown in Figure S1, was found to be indistinguishable from the previously reported SEC data.

Differential Scanning Calorimetry (DSC). DSC experiments were conducted with a TA Q1000 instrument. The sample was rapidly cooled from room temperature to -100 °C and

measurements were collected on heating to 180 °C, cooling to -160 °C, and then reheating to 150 °C at a rate of 10 °C/min. Data can be found in Figure S2. Peaks observed in the derivative of the heat flow at -74 and -127 °C on cooling (Figure S2B) were taken as the glass transition temperatures (T_g) of PEP and PDMS, respectively. On heating, a large exotherm and endotherm were observed at -73 and -44 °C corresponding to the cold crystallization (T_g) and melting temperatures (T_g) of PDMS, respectively.

Small-Angle X-Ray Scattering (SAXS). SAXS measurements were conducted at Sector 5-ID-D of the Advanced Photon Source (APS) at Argonne National Laboratory in Lemont, IL. 1D scattering profiles were obtained by azimuthal integration of 2D scattering patterns. The scattering wavevector $q = 4\pi\lambda^{-1}\sin(\theta/2)$ (θ is the scattering angle and λ is the radiation wavelength) was calibrated using a Au-coated Si diffraction grating with 7200 lines/mm. Samples were hermetically sealed under argon in Tzero DSC pans (DSC Consumables) to prevent degradation, and subjected to various thermal annealing protocols. Scattering data were collected at specified temperatures using either a Linkam DSC600 stage with LN₂ cooling ($T \pm 0.1$ °C) or a custom array heating stage ($T \pm 2$ °C). However, longer annealing experiments were carried out on hotplates ($T \pm 5$ °C) and, for sub-ambient temperatures, in a laboratory freezer ($T = -15 \pm 5$ °C). Prior to measurement, samples annealed at or above room temperature were quickly transferred to the custom array heating stage ($T \pm 10.0$ °C) which was at the desired temperature, and allowed to equilibrate for 5 min. Samples annealed in the laboratory freezer were carried between ice packs to the Linkam stage ($T \pm 10.0$ °C) min, which was again at temperature, and left to equilibrate for 2-5 min prior to measurement.

Dynamic Mechanical Analysis (DMA). Rheological measurements were performed under an inert N_2 atmosphere on an ARES-G2 (TA Instruments) rheometer equipped with 25 mm parallel plates. The sample was disordered at T = 150 °C and cooled to -30 °C at a rate of 0.6 °C/min, after

which isothermal frequency (ω) sweeps were performed every 2 °C approximating a 0.2 °C/min

heating rate. All measurements were conducted with a strain amplitude $\gamma = 1\%$, which strain

sweeps revealed to be well within the linear viscoelastic (LVE) regime (Figure S3). Frequency

data were then shifted according to the time-temperature superposition (TTS) principle by a factor

 $a_{\rm T}$ and corrected for the temperature dependence of the moduli by a factor $b_{\rm T} = \rho(T) T / (\rho(T_{\rm r}) T_{\rm r})$,

where ρ is the density of the copolymer and $T_r = 80$ °C is the chosen reference temperature. Shift

factors are provided in Figure S4. Dynamic elastic (G') and loss (G'') moduli results were

subsequently separated by frequency to produce isochronal temperature ramp data as a function of

frequency. Discontinuities in G' marked order-disorder and order-order transition temperatures

(T_{ODT} and T_{OOT}).

Shear-SAXS. Shear-SAXS measurements were collected at the APS as described above using

a Linkam Cryo CSS450 shear stage with 0.1 °C precision. The sample (~0.5 g) was loaded between

Kapton windows with a gap thickness of 400 μ m and aligned with the shear gradient direction (∇)

parallel to the incident X-ray beam as shown in Figure 5. Shear was applied in an oscillatory mode

with angular frequency ω and strain amplitude γ .

ASSOCIATED CONTENT

The Supporting Information is available free of charge at: [inset url]

Experimental details and additional characterization data (PDF)

AUTHOR INFORMATION

Corresponding Author

37

Frank S. Bates – Department of Chemical Engineering and Materials Science, University of Minnesota, Minnesota, Minnesota 55455, United States; orcid.org/0000-0003-3977-1278; Email: bates001@umn.edu

Authors

Aaron P. Lindsay – Department of Chemical Engineering and Materials Science, University of Minnesota, Minnesota, Minnesota 55455, United States; orcid.org/0000-0003-0223-193X

Ashish Jayaraman – Department of Chemical Engineering and Materials Science, University of Minnesota, Minnesota, Minnesota 55455, United States; orcid.org/0000-0001-7071-7419

Austin J. Peterson – Department of Chemical Engineering and Materials Science, University of Minnesota, Minnesota, Minnesota 55455, United States; orcid.org/0000-0001-8818-1333

Andreas J. Mueller – Department of Chemical Engineering and Materials Science, University of Minnesota, Minnesota, Minnesota 55455, United States; orcid.org/0000-0002-4750-480X

Steven Weigand – DND-CAT Synchrotron Research Center, Northwestern University,

APS/ANL Building 432-A004, 9700 South Cass Ave, Argonne, Illinois 60439, United

States; orcid.org/0000-0003-3137-0672

Kristoffer Almdal – Department of Chemistry, Technical University of Denmark, 2800 Kgs. Lyngby, Denmark; orcid.org/0000-0002-5490-9303

Mahesh K. Mahanthappa – Department of Chemical Engineering and Materials Science,
University of Minnesota, Minneapolis, Minnesota 55455, United States; orcid.org/00000002-9871-804X

Timothy P. Lodge – Department of Chemical Engineering and Materials Science and Department of Chemistry, University of Minnesota, Minneapolis, Minnesota 55455, United States; orcid.org/0000-0001-5916-8834

Author Contributions

The manuscript was written through contributions of all authors. A.P.L., F.S.B., and K.A. identified the previous report on the PEP-PDMS copolymer used in this study and K.A. provided the sample. A.P.L, A.J., and S.W. performed the SAXS experiments. A.P.L. and A.J.P. conducted the DMA experiments. A.J.M. carried out the DSC measurements. The experimental data was analyzed by A.P.L and A.J., and A.P.L. drafted the manuscript. F.S.B, M.K.M, and T.P.L. supervised the overall project. All authors have given approval to the final version of the manuscript and the supporting information.

Funding Sources

This work was supported by the National Science Foundation under Grants No. DMR-1801993 (A.P.L., A.J.M., F.S.B.) and CHE-1807330 (A.J., M.K.M.) as well as a National Science Foundation Graduate Research Fellowship under Grant No. 00039202 (A.P.L.).

Notes

The authors declare no competing financial interest.

ACKNOWLEDGMENTS

We would like to express our thanks to all the staff at Sector 5 who provided invaluable help in conducting these experiments, keeping science moving forward in spite of the ongoing pandemic. SAXS experiments were performed at the DuPont-Northwestern-Dow Collaborative Access Team (DND-CAT) located at Sector 5 of the Advanced Photon Source (APS). DND-CAT is supported by Northwestern University, The Dow Chemical Company, and DuPont de Nemours, Inc. This research used resources of the Advanced Photon Source, a U.S. Department of Energy (DOE) Office of Science User Facility operated for the DOE Office of Science by Argonne National Laboratory under Contract No. DE-AC02-06CH11357. Data was collected using an instrument funded by the National Science Foundation under Award Number 0960140.

REFERENCES

- (1) Lee, S.; Bluemle, M. J.; Bates, F. S. Discovery of a Frank-Kasper σ Phase in Sphere-Forming Block Copolymer Melts. *Science* **2010**, *330*, 349–353. https://doi.org/10.1126/science.1195552.
- (2) Kim, K.; Schulze, M. W.; Arora, A.; Lewis, R. M.; Hillmyer, M. A.; Dorfman, K. D.; Bates, F. S. Thermal Processing of Diblock Copolymer Melts Mimics Metallurgy. *Science* **2017**, *356*, 520–523. https://doi.org/10.1126/science.aam7212.
- (3) Bates, M. W.; Lequieu, J.; Barbon, S. M.; Lewis, R. M.; Delaney, K. T.; Anastasaki, A.; Hawker, C. J.; Fredrickson, G. H.; Bates, C. M. Stability of the A15 Phase in Diblock Copolymer Melts. *Proc. Natl. Acad. Sci. U. S. A.* **2019**, *116*, 13194–13199. https://doi.org/10.1073/pnas.1900121116.
- (4) Uddin, M. H.; Rodriguez, C.; López-Quintela, A.; Leisner, D.; Solans, C.; Esquena, J.;
 Kunieda, H. Phase Behavior and Microstructure of

- Poly(Oxyethylene)—Poly(Dimethylsiloxane) Copolymer Melt. *Macromolecules* **2003**, *36*, 1261–1271. https://doi.org/10.1021/ma0210978.
- (5) Gillard, T. M.; Lee, S.; Bates, F. S. Dodecagonal Quasicrystalline Order in a Diblock Copolymer Melt. *Proc. Natl. Acad. Sci. U. S. A.* **2016**, *113*, 5167–5172. https://doi.org/10.1073/pnas.1601692113.
- (6) Bates, F. S.; Cohen, R. E.; Berney, C. V. Small-Angle Neutron Scattering Determination of Macrolattice Structure in a Polystyrene-Polybutadiene Diblock Copolymer.

 *Macromolecules** 1982, 15, 589–592. https://doi.org/10.1021/ma00230a073.
- Lewis, R. M.; Arora, A.; Beech, H. K.; Lee, B.; Lindsay, A. P.; Lodge, T. P.; Dorfman, K. D.; Bates, F. S. Role of Chain Length in the Formation of Frank-Kasper Phases in Diblock Copolymers. *Phys. Rev. Lett.* 2018, 121, 208002. https://doi.org/10.1103/PhysRevLett.121.208002.
- (8) Xie, N.; Li, W.; Qiu, F.; Shi, A. C. σ Phase Formed in Conformationally Asymmetric AB-Type Block Copolymers. *ACS Macro Lett.* **2014**, *3*, 909–910. https://doi.org/10.1021/mz500445v.
- (9) Schulze, M. W.; Lewis, R. M.; Lettow, J. H.; Hickey, R. J.; Gillard, T. M.; Hillmyer, M. A.; Bates, F. S. Conformational Asymmetry and Quasicrystal Approximants in Linear Diblock Copolymers. *Phys. Rev. Lett.* 2017, 118, 207801. https://doi.org/10.1103/PhysRevLett.118.207801.

- (10) Chang, A. B.; Bates, F. S. Impact of Architectural Asymmetry on Frank-Kasper Phase Formation in Block Polymer Melts. *ACS Nano* **2020**, *14*, 11463–11472. https://doi.org/10.1021/acsnano.0c03846.
- (11) Bates, M. W.; Barbon, S. M.; Levi, A. E.; Lewis, R. M.; Beech, H. K.; Vonk, K. M.; Zhang, C.; Fredrickson, G. H.; Hawker, C. J.; Bates, C. M. Synthesis and Self-Assembly of AB_n Miktoarm Star Polymers. *ACS Macro Lett.* 2020, 9, 396–403. https://doi.org/10.1021/acsmacrolett.0c00061.
- (12) Sun, Y.; Tan, R.; Ma, Z.; Gan, Z.; Li, G.; Zhou, D.; Shao, Y.; Zhang, W. Bin; Zhang, R.; Dong, X. H. Discrete Block Copolymers with Diverse Architectures: Resolving Complex Spherical Phases with One Monomer Resolution. ACS Cent. Sci. 2020, 6, 1386–1393. https://doi.org/10.1021/acscentsci.0c00798.
- Yue, K.; Huang, M.; Marson, R. L.; Hec, J.; Huang, J.; Zhou, Z.; Wang, J.; Liu, C.; Yan, X.; Wu, K.; Guo, Z.; Liu, H.; Zhang, W.; Ni, P.; Wesdemiotis, C.; Zhang, W. B.; Glotzer, S. C.; Cheng, S. Z. D. Geometry Induced Sequence of Nanoscale Frank-Kasper and Quasicrystal Mesophases in Giant Surfactants. *Proc. Natl. Acad. Sci. U. S. A.* 2016, *113*, 14195–14200. https://doi.org/10.1073/pnas.1609422113.
- (14) Hudson, S. D.; Jung, H. T.; Percec, V.; Cho, W. D.; Johansson, G.; Ungar, G.; Balagurusamy, V. S. K. Direct Visualization of Individual Cylindrical and Spherical Supramolecular Dendrimers. *Science* 1997, 278, 449–452. https://doi.org/10.1126/science.278.5337.449.
- (15) Mueller, A. J.; Lindsay, A. P.; Jayaraman, A.; Lodge, T. P.; Mahanthappa, M. K.; Bates,F. S. Quasicrystals and Their Approximants in a Crystalline-Amorphous Diblock

- Copolymer. *Macromolecules* **2021**, *54*, 2647–2660. https://doi.org/10.1021/acs.macromol.0c02871.
- (16) Takagi, H.; Hashimoto, R.; Igarashi, N.; Kishimoto, S.; Yamamoto, K. Frank-Kasper σ Phase in Polybutadiene-Poly(ε-Caprolactone) Diblock Copolymer/Polybutadiene Blends. *J. Phys. Condens. Matter* 2017, 29, 204002. https://doi.org/10.1088/1361-648X/aa6908.
- (17) Takagi, H.; Yamamoto, K. Phase Boundary of Frank-Kasper σ Phase in Phase Diagrams of Binary Mixtures of Block Copolymers and Homopolymers. *Macromolecules* **2019**, *52*, 2007–2014. https://doi.org/10.1021/acs.macromol.8b02356.
- (18) Liu, M.; Qiang, Y.; Li, W.; Qiu, F.; Shi, A. C. Stabilizing the Frank-Kasper Phases *via*Binary Blends of AB Diblock Copolymers. *ACS Macro Lett.* **2016**, *5*, 1167–1171.

 https://doi.org/10.1021/acsmacrolett.6b00685.
- (19) Lindsay, A. P.; Lewis, R. M.; Lee, B.; Peterson, A. J.; Lodge, T. P.; Bates, F. S. A15, σ, and a Quasicrystal: Access to Complex Particle Packings *via* Bidisperse Diblock Copolymer Blends. *ACS Macro Lett.* **2020**, *9*, 197–203. https://doi.org/10.1021/acsmacrolett.9b01026.
- Mueller, A. J.; Lindsay, A. P.; Jayaraman, A.; Lodge, T. P.; Mahanthappa, M. K.; Bates,
 F. S. Emergence of a C15 Laves Phase in Diblock Polymer/Homopolymer Blends. ACS
 Macro Lett. 2020, 9, 576–582. https://doi.org/10.1021/acsmacrolett.0c00124.
- (21) Cheong, G. K.; Bates, F. S.; Dorfman, K. D. Symmetry Breaking in Particle-Forming Diblock Polymer/Homopolymer Blends. *Proc. Natl. Acad. Sci. U. S. A.* **2020**, *117*, 16764–16769. https://doi.org/10.1073/pnas.2006079117.

- (22) Xie, S.; Lindsay, A. P.; Bates, F. S.; Lodge, T. P. Formation of a C15 Laves Phase with a Giant Unit Cell in Salt-Doped A/B/AB Ternary Polymer Blends. *ACS Nano* **2020**, *14*, 13754–13764. https://doi.org/10.1021/acsnano.0c06071.
- (23) Xie, J.; Shi, A.-C. Formation of Complex Spherical Packing Phases in Diblock Copolymer/Homopolymer Blends. *Giant* **2021**, *5*, 100043. https://doi.org/10.1016/j.giant.2020.100043.
- (24) Baez-Cotto, C. M.; Mahanthappa, M. K. Micellar Mimicry of Intermetallic C14 and C15 Laves Phases by Aqueous Lyotropic Self-Assembly. *ACS Nano* **2018**, *12*, 3226–3234. https://doi.org/10.1021/acsnano.7b07475.
- (25) Liu, Y.; Liu, T.; Yan, X.; Guo, Q.-Y.; Wang, J.; Zhang, R.; Zhang, S.; Su, Z.; Huang, J.; Liu, G.-X.; Zhang, W.; Zhang, W.; Aida, T.; Yue, K.; Huang, M.; Cheng, S. Z. D. Mesoatom Alloys via Self-Sorting Approach of Giant Molecules Blends. Giant 2020, 4, 100031. https://doi.org/10.1016/j.giant.2020.100031.
- (26) Bates, F. S.; Berney, C. V.; Cohen, R. E. Microphase Structure of Solvent-Cast Diblock Copolymers and Copolymer-Homopolymer Blends Containing Spherical Microdomains.

 *Macromolecules** 1983, 16, 1101–1108. https://doi.org/10.1021/ma00241a011.
- (27) Tanaka, H.; Hascgawa, H.; Hashimoto, T. Ordered Structure in Mixtures of a Block Copolymer and Homopolymers. 1. Solubilization of Low Molecular Weight Homopolymers. *Macromolecules* 1991, 24, 240–251. https://doi.org/10.1021/ma00001a037.

- (28) Hashimoto, T.; Koizumi, S.; Hasegawa, H. Ordered Structure in Blends of Block Copolymers. 2. Self-Assembly for Immiscible Lamella-Forming Copolymers.

 *Macromolecules** 1994, 27, 1562–1570. https://doi.org/10.1021/ma00084a043.
- (29) Koizumi, S.; Hasegawa, H.; Hashimoto, T. Ordered Structure in Blends of Block Copolymers. 3. Self-Assembly in Blends of Sphere- or Cylinder-Forming Copolymers.

 *Macromolecules** 1994, 27, 4371–4381. https://doi.org/10.1021/ma00093a044.
- (30) Spontak, R. J.; Fung, J. C.; Braunfeld, M. B.; Sedat, J. W.; Agard, D. A.; Kane, L.; Smith, S. D.; Satkowski, M. M.; Ashraf, A.; Hajduk, D. A.; Gruner, S. M. Phase Behavior of Ordered Diblock Copolymer Blends: Effect of Compositional Heterogeneity. *Macromolecules* 1996, 29, 4494–4507. https://doi.org/10.1021/ma9515689.
- (31) Vilesov, A. D.; Floudas, G.; Pakula, T.; Melenevskaya, E. Y.; Birshtein, T. M.; Lyatskaya, Y. V. Lamellar Structure Formation in the Mixture of Two Cylinder-Forming Block Copolymers. *Macromol. Chem. Phys.* 1994, 195, 2317–2326. https://doi.org/10.1002/macp.1994.021950704.
- (32) Hashimoto, T.; Tanaka, H.; Hasegawa, H. Ordered Structure in Mixtures of a Block Copolymer and Homopolymers. 2. Effects of Molecular Weights of Homopolymers.

 *Macromolecules** 1990, 23, 4378–4386. https://doi.org/10.1021/ma00222a009.
- (33) Winey, K. I.; Thomas, E. L.; Fetters, L. J. Ordered Morphologies in Binary Blends of Diblock Copolymer and Homopolymer and Characterization of Their Intermaterial Dividing Surfaces. J. Chem. Phys. 1991, 95, 9367–9375. https://doi.org/10.1063/1.461164.

- (34) Lodge, T. P.; Pudil, B.; Hanley, K. J. The Full Phase Behavior for Block Copolymers in Solvents of Varying Selectivity. *Macromolecules* **2002**, *35*, 4707–4717. https://doi.org/10.1021/ma0200975.
- (35) Grosius, P. P.; Gallot, Y.; Skoulios, A. Copolymeres Séquencés Polystyrène/Polyvinyl-4
 Pyridine: Synthèse, Caractérisation et Étude Des Phases Mésomorphes. *Die Makromol.*Chemie 1970, 132, 35–55. https://doi.org/10.1002/macp.1970.021320104.
- (36) Clerc, M. A New Symmetry for the Packing of Amphiphilic Direct Micelles. *J. Phys. II*Fr. 1996, 6, 961–968. https://doi.org/10.1051/jp2:1996110.
- (37) Sakya, P.; Seddon, J. M.; Templer, R. H.; Mirkin, R. J.; Tiddy, G. J. T. Micellar Cubic Phases and Their Structural Relationships: The Nonionic Surfactant System C12EO12/Water. *Langmuir* **1997**, *13*, 3706–3714. https://doi.org/10.1021/la9701844.
- (38) Imai, M.; Yoshida, I.; Iwaki, T.; Nakaya, K. Static and Dynamic Structures of Spherical Nonionic Surfactant Micelles during the Disorder-Order Transition. *J. Chem. Phys.* **2005**, *122*, 044906. https://doi.org/10.1063/1.1839559.
- (39) Hashimoto, T.; Yamasaki, K.; Koizumi, S.; Hasegawa, H. Ordered Structure in Blends of Block Copolymers. 1. Miscibility Criterion for Lamellar Block Copolymers.

 *Macromolecules** 1993, 26, 2895–2904. https://doi.org/10.1021/ma00063a039.
- Jayaraman, A.; Zhang, D. Y.; Dewing, B. L.; Mahanthappa, M. K. Path-Dependent Preparation of Complex Micelle Packings of a Hydrated Diblock Oligomer. *ACS Cent. Sci.*2019, 5 (4), 619–628. https://doi.org/10.1021/acscentsci.8b00903.

- (41) Papadakis, C. M.; Almdal, K.; Mortensen, K.; Vigild, M. E.; Štěpánek, P. Unexpected Phase Behavior of an Asymmetric Diblock Copolymer. *J. Chem. Phys.* **1999**, *111*, 4319–4326. https://doi.org/10.1063/1.479730.
- (42) Fetters, L. J.; Lohse, D. J.; Richter, D.; Witten, T. A.; Zirkel, A. Connection between Polymer Molecular Weight, Density, Chain Dimensions, and Melt Viscoelastic Properties.

 *Macromolecules** 1994, 27, 4639–4647. https://doi.org/10.1021/ma00095a001.
- (43) Duan, C.; Zhao, M.; Qiang, Y.; Chen, L.; Li, W.; Qiu, F.; Shi, A. C. Stability of Two-Dimensional Dodecagonal Quasicrystalline Phase of Block Copolymers. *Macromolecules* **2018**, *51*, 7713–7721. https://doi.org/10.1021/acs.macromol.8b01638.
- (44) Ungar, G.; Liu, Y.; Zeng, X.; Percec, V.; Cho, W.-D. Giant Supramolecular Liquid Crystal Lattice. *Science* **2003**, *299*, 1208–1211. https://doi.org/10.1007/springerreference 11442.
- (45) Zeng, X.; Ungar, G.; Liu, Y.; Percec, V.; Dulcey, A. E.; Hobbs, J. K. Supramolecular Dendritic Liquid Quasicrystals. *Nature* **2004**, *428*, 157–160. https://doi.org/10.1038/nature02368.
- (46) Lee, S.; Gillard, T. M.; Bates, F. S. Fluctuations, Order, and Disorder in Short Diblock Copolymers. *AIChE J.* **2013**, *59*, 3502–3513. https://doi.org/10.1002/aic.
- (47) Lee, S. Structure and Dynamics of Block Copolymer Based Soft Materials. Ph.D. Thesis, University of Minnesota, Minneapolis, MN, 2011.
- (48) Gillard, T. M. Phase Transitions and Fluctuations in Block Copolymer-Based Soft Materials. Ph.D. Thesis, University of Minnesota, Minneapolis, MN, 2015.

- (49) Kossuth, M. B.; Morse, D. C.; Bates, F. S. Viscoelastic Behavior of Cubic Phases in Block Copolymer Melts. *J. Rheol.* **1999**, *43* (1), 167–196. https://doi.org/10.1122/1.550981.
- (50) Valentine, C. S.; Walker, L. M. Rheological Characterization of BCC and FCC Structures in Aqueous Diblock Copolymer Liquid Crystals. *Korea Aust. Rheol. J.* **2019**, *31*, 249–254. https://doi.org/10.1007/s13367-019-0025-2.
- (51) Kraynik, A. M.; Reinelt, D. A. Linear Elastic Behavior of Dry Soap Foams. *J. Colloid Interface Sci.* **1996**, *181*, 511–520. https://doi.org/10.1006/jcis.1996.0408.
- (52) Treitschke, W.; Tammann, G. Über Die Legierungen Des Eisens Mit Chrom. *Zeitschrift für Anorg. Chemie* **1907**, *55*, 402–411. https://doi.org/doi.org/10.1002/zaac.19070550131.
- (53) Bain, E. C.; Griffiths, W. E. An Introduction to the Iron-Chromium-Nickel Alloys. *Trans.*AIME 1927, 75, 166–211.
- (54) Bergman, B. G.; Shoemaker, D. P. The Space Group of the σ-FeCr Crystal Structure. *J. Chem. Phys.* **1951**, *19*, 515. https://doi.org/10.1063/1.1748278.
- (55) Bergman, G.; Shoemaker, D. P. The Determination of the Crystal Structure of the σ Phase in the Iron–Chromium and Iron–Molybdenum Systems. *Acta Crystallogr.* **1954**, *7*, 857–865. https://doi.org/10.1107/s0365110x54002605.
- (56) Armstrong, P. E.; Eash, D. T.; Hockett, J. E. Elastic Moduli of Alpha, Beta and Gamma Polycrystalline Uranium. *J. Nucl. Mater.* **1972**, *45*, 211–216. https://doi.org/10.1016/0022-3115(72)90167-5.
- (57) Holden, A. N. Physical Metallurgy of Uranium; Addison-Wesley Publishing Co.: Reading, Mass., USA, 1958.

- (58) Hall, E. O.; Algie, S. H. The Sigma Phase. *Metall. Rev.* **1966**, *11*, 61–88. https://doi.org/https://doi.org/10.1179/mtlr.1966.11.1.61.
- (59) Cavicchi, K. A.; Lodge, T. P. Domain Size Equilibration in Sphere-Forming Block Copolymers. *J. Polym. Sci. Part B Polym. Phys.* **2003**, *41*, 715–724. https://doi.org/10.1002/polb.10427.
- (60) Almdal, K.; Koppi, K. A.; Bates, F. S. Dynamically Sheared Body-Centered-Cubic Ordered Diblock Copolymer Melt. *Macromolecules* **1993**, *26*, 4058–4060. https://doi.org/10.1021/ma00067a053.
- (61) Koppi, K. A.; Tirrell, M.; Bates, F. S.; Almdal, K.; Mortensen, K. Epitaxial Growth and Shearing of the Body Centered Cubic Phase in Diblock Copolymer Melts. *J. Rheol.* **1994**, 38, 999–1027. https://doi.org/10.1122/1.550600.
- (62) Almdal, K.; Mortensen, K.; Ryan, A. J.; Bates, F. S. Order, Disorder, and Composition Fluctuation Effects in Low Molar Mass Hydrocarbon-Poly(Dimethylsiloxane) Diblock Copolymers. *Macromolecules* **1996**, *29*, 5940–5947. https://doi.org/10.1021/ma960437k.
- (63) Amos, R. M.; Rarity, J. G.; Tapster, P. R.; Shepherd, T. J.; Kitson, S. C. Fabrication of Large-Area Face-Centered-Cubic Hard-Sphere Colloidal Crystals by Shear Alignment. *Phys. Rev. E Stat. Physics, Plasmas, Fluids, Relat. Interdiscip. Top.* **2000**, *61*, 2929–2935. https://doi.org/10.1103/PhysRevE.61.2929.
- (64) López-Barrón, C. R.; Wagner, N. J.; Porcar, L. Layering, Melting, and Recrystallization of a Close-Packed Micellar Crystal under Steady and Large-Amplitude Oscillatory Shear Flows. J. Rheol. 2015, 59, 793–820. https://doi.org/10.1122/1.4917542.

- (65) Ruiz-Franco, J.; Marakis, J.; Gnan, N.; Kohlbrecher, J.; Gauthier, M.; Lettinga, M. P.; Vlassopoulos, D.; Zaccarelli, E. Crystal-to-Crystal Transition of Ultrasoft Colloids under Shear. *Phys. Rev. Lett.* 2018, 120, 78003. https://doi.org/10.1103/PhysRevLett.120.078003.
- (66) Hong, Y. R.; Adamson, D. H.; Chaikin, P. M.; Register, R. A. Shear-Induced Sphere-to-Cylinder Transition in Diblock Copolymer Thin Films. *Soft Matter* 2009, 5, 1687–1691. https://doi.org/10.1039/b820312a.
- (67) Schulz, M. F.; Bates, F. S.; Almdal, K.; Mortensen, K. Epitaxial Relationship for Hexagonal-to-Cubic Phase Transition in a Block Copolymer Mixture. *Phys. Rev. Lett.* 1994, 73, 86–89. https://doi.org/10.1103/PhysRevLett.73.86.
- (68) Taylor, G. I. The Deformation of Crystals of β-Brass. *Proc. R. Soc. London* **1928**, *118*, 1–24. https://doi.org/https://doi.org/10.1098/rspa.1928.0032.
- (69) Gough, H. The Behavior of a Single Crystal of α-Iron Subjected to Alternating Torsional Stresses. Proc. R. Soc. London 1928, 118, 498–534. https://doi.org/10.1098/rspa.1930.0069.
- (70) Weinberger, C. R.; Boyce, B. L.; Battaile, C. C. Slip Planes in BCC Transition Metals. *Int. Mater. Rev.* 2013, 58, 296–314. https://doi.org/10.1179/1743280412Y.0000000015.
- Holden, A. N. Growth and Crystallography of Deformation of β-Phase Uranium Single
 Crystals. Acta Crystallogr. 1952, 5, 182–184.
 https://doi.org/10.1107/s0365110x52000538.

- (72) Kronberg, M. L. Atom Movements and Dislocation Structures for Plastic Slip in Single Crystals of β-Uranium. *J. Nucl. Mater.* **1959**, *1*, 85–95. https://doi.org/10.1016/0022-3115(59)90013-3.
- (73) Rodriguez, C.; Coll, J. A. Deformation Mechanisms of β Uranium Single Crystals. *J. Nucl. Mater.* **1964**, *11*, 212–219. https://doi.org/10.1007/978-3-662-08734-3 3.
- (74) Marcinkowski, M. J.; Miller, D. S. A Study of Defect Sub-Structures in the Fe–Cr Sigma Phase by Means of Transmission Electron Microscopy. *Philos. Mag.* 1962, 7, 1025–1059. https://doi.org/10.1080/14786436208212898.
- (75) Kitchingman, W. J. The Atomic Mechanism of the Body-Centred Cubic to σ Phase Transformation. *Acta Crystallogr. Sect. A* **1968**, 24, 282–286. https://doi.org/10.1107/S056773946800046X.
- (76) Lee, S.; Leighton, C.; Bates, F. S. Sphericity and Symmetry Breaking in the Formation of Frank-Kasper Phases from One Component Materials. *Proc. Natl. Acad. Sci. U. S. A.* 2014, 111, 17723–17731. https://doi.org/10.1073/pnas.1408678111.
- (77) Zhang, Y.; Du, K.; Zhang, W.; Du, B.; Qi, D.; Li, W.; Song, M.; Sheng, L.; Ye, H. Shear Deformation Determined by Short-Range Configuration of Atoms in Topologically Close-Packed Crystal. *Acta Mater.* 2019, 179, 396–405. https://doi.org/10.1016/j.actamat.2019.08.056.
- Wollgarten, M.; Beyss, M.; Urban, K.; Liebertz, H.; Köster, U. Direct Evidence for Plastic
 Deformation of Quasicrystals by Means of a Dislocation Mechanism. *Phys. Rev. Lett.* 1993, 71, 549–552. https://doi.org/10.1103/PhysRevLett.71.549.

- (79) Mikulla, R.; Roth, J.; Trebin, H. R. Simulation of Shear Stress in Two-Dimensional Decagonal Quasicrystals. *Philos. Mag. B Phys. Condens. Matter; Stat. Mech. Electron.* Opt. Magn. Prop. 1995, 71, 981–989. https://doi.org/10.1080/01418639508243601.
- (80) Peterca, M.; Imam, M. R.; Hudson, S. D.; Partridge, B. E.; Sahoo, D.; Heiney, P. A.; Klein, M. L.; Percec, V. Complex Arrangement of Orthogonal Nanoscale Columns via a Supramolecular Orientational Memory Effect. ACS Nano 2016, 10, 10480–10488. https://doi.org/10.1021/acsnano.6b06419.
- (81) Fischer, S.; Exner, A.; Zielske, K.; Perlich, J.; Deloudi, S.; Steurer, W.; Lindner, P.; Förstere, S. Colloidal Quasicrystals with 12-Fold and 18-Fold Diffraction Symmetry. *Proc. Natl. Acad. Sci. U. S. A.* 2011, 108, 1810–1814. https://doi.org/10.1073/pnas.1008695108.
- (82) Park, M. J.; Bang, J.; Harada, T.; Char, K.; Lodge, T. P. Epitaxial Transitions among FCC, HCP, BCC, and Cylinder Phases in a Block Copolymer Solution. *Macromolecules* **2004**, *37*, 9064–9075. https://doi.org/10.1021/ma049285g.
- (83) Andersson, S. Structures Related to the β-Tungsten or Cr₃Si Structure Type. *J. Solid State Chem.* **1978**, *23*, 191–204. https://doi.org/10.1016/0022-4596(78)90065-8.
- (84) Stampfli, P. A Dodecagonal Quasi-Periodic Lattice in 2 Dimensions. *Helv. Phys. Acta* **1986**, *59*, 1260–1263.
- (85) Baake, M.; Klitzing, R.; Schlottmann, M. Fractally Shaped Acceptance Domains of Quasiperiodic Square-Triangle Tilings with Dodecagonal Symmetry. *Phys. A Stat. Mech. its Appl.* **1992**, *191*, 554–558. https://doi.org/10.1016/0378-4371(92)90582-B.

- (86) Zhang, R.; Zeng, X.; Ungar, G. Direct AFM Observation of Individual Micelles, Tile Decorations and Tiling Rules of a Dodecagonal Liquid Quasicrystal. *J. Phys. Condens.*Matter 2017, 29 (41). https://doi.org/10.1088/1361-648X/aa818a.
- (87) Zurkirch, M.; Bolliger, B.; Erbudak, M.; Kortan, A. R. Structural Transformations at the Surface of the Decagonal Quasicrystal Al₇₀Co₁₅Ni₁₅. *Phys. Rev. B* **1998**, *58*, 14113–14116.
- (88) Bolliger, B.; Erbudak, M.; Vvedensky, D. D.; Zurkirch, M.; Kortan, A. R. Surface Structural Transitions on the Icosahedral Quasicrystal Al70Pd20Mn10. *Phys. Rev. Lett.* 1998, 80, 5369–5372. https://doi.org/10.1103/PhysRevLett.80.5369.
- (89) Widjaja, E. J.; Marks, L. D. Models for Quasicrystal-Crystal Epitaxy. J. Phys. Condens.
 Matter 2008, 20, 314003. https://doi.org/10.1088/0953-8984/20/31/314003.
- (90) Zhang, R.; Zeng, X.; Ungar, G. Direct AFM Observation of Individual Micelles, Tile Decorations and Tiling Rules of a Dodecagonal Liquid Quasicrystal. *J. Phys. Condens.* Matter 2017, 29, 414001. https://doi.org/10.1088/1361-648X/aa818a.
- (91) Hamley, I. W.; Pople, J. A.; Fairclough, J. P. A.; Ryan, A. J.; Booth, C.; Yang, Y. W. Shear-Induced Orientational Transitions in the Body-Centered Cubic Phase of a Diblock Copolymer Gel. *Macromolecules* 1998, 31, 3906–3911. https://doi.org/10.1021/ma971561m.
- (92) Ishimasa, T.; Kitano, Y.; Komura, Y. Faulted Structure in the Fe–Cr σ Phase. *Phys. Status Solidi* **1981**, *66*, 703–715. https://doi.org/10.1002/pssa.2210660236.
- (93) Lewis, R. M.; Beech, H. K.; Jackson, G. L.; Maher, M. J.; Kim, K.; Narayanan, S.; Lodge, T. P.; Mahanthappa, M. K.; Bates, F. S. Dynamics of a Supercooled Disordered Sphere-

- Forming Diblock Copolymer as Determined by X-Ray Photon Correlation and Dynamic Mechanical Spectroscopies. *ACS Macro Lett.* **2018**, 7, 1486–1491. https://doi.org/10.1021/acsmacrolett.8b00740.
- (94) Feng, X.; Liu, G.; Guo, D.; Lang, K.; Zhang, R.; Huang, J.; Su, Z.; Li, Y.; Huang, M.; Li, T.; Cheng, S. Z. D. Transition Kinetics of Self-Assembled Supramolecular Dodecagonal Quasicrystal and Frank-Kasper σ Phases in AB_n Dendron-Like Giant Molecules. ACS Macro Lett. 2019, 8, 875–881. https://doi.org/10.1021/acsmacrolett.9b00287.
- (95) Huang, Y.-Y.; Hsu, J.-Y.; Chen, H.-L.; Hashimoto, T. Existence of FCC-Packed Spherical Micelles in Diblock Copolymer Melt. *Macromolecules* 2007, 40, 406–409. https://doi.org/10.1021/ma062149m.
- (96) Hsu, N. W.; Nouri, B.; Chen, L. T.; Chen, H. L. Hexagonal Close-Packed Sphere Phase of Conformationally Symmetric Block Copolymer. *Macromolecules* 2020, 53, 9665–9675. https://doi.org/10.1021/acs.macromol.0c01445.
- (97) Vardeny, Z. V.; Nahata, A.; Agrawal, A. Optics of Photonic Quasicrystals. *Nat. Photonics* **2013**, 7, 177–184. https://doi.org/10.1038/nphoton.2012.343.
- (98) Klatt, M. A.; Steinhardt, P. J.; Torquato, S. Phoamtonic Designs Yield Sizeable 3D Photonic Band Gaps. Proc. Natl. Acad. Sci. U. S. A. 2019, 116, 23480–23486. https://doi.org/10.1073/pnas.1912730116.
- (99) Park, M.; Harrison, C.; Chaikin, P. M.; Register, R. A.; Adamson, D. H. Block Copolymer Lithography: Periodic Arrays of ~10¹¹ Holes in 1 Square Centimeter. *Science* **1997**, *276*, 1401–1404. https://doi.org/10.1126/science.276.5317.1401.

- (100) Ren, J.; Segal-Peretz, T.; Zhou, C.; Craig, G. S. W.; Nealey, P. F. Three-Dimensional Superlattice Engineering with Block Copolymer Epitaxy. *Sci. Adv.* **2020**, *6*, 1–8. https://doi.org/10.1126/sciadv.aaz0002.
- (101) Vigild, M. E. Mesomorphic Phase Behaviour of Low Molar Mass PEP-PDMS Diblock Copolymers Synthesized by Anionic Polymerization. Ph.D. Thesis, University of Copenhagen, Copenhagen, Denmark, 1997.